

8644

JNCASR
532.51 P07



Direct numerical simulation of transition in unstably stratified Poiseuille flow

A Thesis

Submitted for the Degree of

MASTER OF SCIENCE (ENGINEERING)

by

KAUSHIK SRINIVASAN



ENGINEERING MECHANICS UNIT
JAWAHARLAL NEHRU CENTRE FOR ADVANCED SCIENTIFIC
RESEARCH

(A Deemed University)

Bangalore – 560 064

DECEMBER 2007

To my Father

532.51
Poa

DECLARATION


I hereby declare that the matter embodied in the thesis entitled “**Direct numerical simulation of transition in unstably stratified Poiseuille flow**” is the result of investigations carried out by me at the Engineering Mechanics Unit, Jawaharlal Nehru Centre for Advanced Scientific Research, Bangalore, India under the supervision of Prof. Rama Govindarajan and that it has not been submitted elsewhere for the award of any degree or diploma.

In keeping with the general practice in reporting scientific observations, due acknowledgment has been made whenever the work described is based on the findings of other investigators.

Kaushik Srinivasan

CERTIFICATE

I hereby certify that the matter embodied in this thesis entitled "**Direct numerical simulation of transition in unstably stratified Poiseuille flow**" has been carried out by Mr. Kaushik Srinivasan at the Engineering Mechanics Unit, Jawaharlal Nehru Centre for Advanced Scientific Research, Bangalore, India under my supervision and that it has not been submitted elsewhere for the award of any degree or diploma.


Prof. Rama Govindarajan
(Research Supervisor)

Acknowledgements

Prof. Rama Govindarajan, my advisor, for all the guidance in research, of course, but also for all the friendly advice that I might have needed every now and then. Did I mention showing the massive amount of tolerance and patience needed in guiding me?

Prof. Roddam Narasimha, for teaching me the care and meticulousness that scientific research needs. that nothing can be taken for granted.

Prof. Timothy Poston, for rekindling my interest in pure mathematics and rigor, something that I had long thought lost.

My dad and mom, for instilling me an interest in science in the purest sense, well removed from the brahminical notions of education.

My wonderfully sensible sweet mother, from whom I've inherited almost every mental trait, except her sweetness and of course, her good sense.

Supraja, my sister- for being my travel agent, banker, troubleshooter, friend and a million other things. For supporting me to an extent that I have no reason to expect or deserve.

Komala Ramachandra, for being a catalyst in the immeasurable level of perspective that I have gained in the past two years, and for making me a better person.

Sriram ananth, for sharing duties with my sister in event managing me, for no fault of his.

Pinaki Bhattacharya, for being a friend and for dishing out that sarcastic bit of sense (which is of course the only way to communicate) when I needed it most but wanted it the least.

Vivek, for ferrying me around for my thesis printing when I needed it most (and for making sure the acknowledgement was placed this high)...

Anubhab and Ratul for being the other half of the crazy four.

Rajaram and Vijay for being really good friends.

Mukund, Harish, Vinod, Sameen, Antina, Vineeta, Rajapandiyam, Bishakh and others who I have forgotten to acknowledge though are probably irrelevant...

The Engineering Mechanics Unit, for being a maniacal, impossible, intolerable, unreal meanie. But also for being an air-conditioned oasis in the middle of the desert. And speaking of air-conditioning...

Kirti, for making it possible to use, "frozen to the teeth" and "summer" in the same sentence without ending up with an oxymoron.

And of course, the Many denizens of JNCASR, for providing all the entertainment over the past two years, albeit unwittingly...

Abstract

In the present study, we have implemented a three-dimensional direct numerical simulation (DNS) algorithm for the purpose of studying instability and transition in a Poiseuille flow with imposed unstable stratification. We are specifically interested in studying the algebraic instability mechanism as a route to transition and the effect of stratification on the same.

The DNS uses a mixed finite-difference-spectral algorithm that embodies a sixth order central difference scheme in the wall normal direction and spectral Fourier method in the spanwise and streamwise directions, which are taken to be periodic. We first establish the validity of the DNS code in the present context by verification of the results obtained from the DNS with that obtained from linear theory, both in the case of modal theory and transient growth. In the former case we show that the DNS captures the growth rate and frequency of an input disturbance, which is in the form of the most unstable eigenfunction, quite accurately. We then study the evolution of optimal perturbations of small amplitudes and show that the energy evolution curves, in comparison with linear theory, are captured well by the DNS, as is the evolution of the actual flow field.

Our next step is to consider the evolution of a finite amplitude optimal perturbation in three dimensions which are in the form of streamwise vortices, with and without the presence of unstable stratification. We find that the optimal perturbations redistribute mean shear to form streaks which are organized regions of high and low speed fluid relative to the background mean profile. A similar mechanism is shown to redistribute the mean temperature profile to form high and low intensity temperature streaks. We first consider the evolution of the energy of the perturbation and find that the energy evolves in two different growth spurts before decaying eventually. By analyzing the temperature and flow fields, which are presented at various times in considerable detail, we are able to observe the basic mechanism of the streak instability process. We then compare the nature

of streak instability process with and without the presence of stratification and consider possible reasons - both physical and computational, for the observations.

List of Figures

2.1	Schematic of a stratified channel flow.	8
2.2	Schematic of the projection method the evolution of the velocity field with time. $\mathbf{u}_{\text{exact}}$, \mathbf{u} and $\tilde{\mathbf{u}}$ are the exact velocity field (<i>i.e.</i> the solution of the continuous system, the divergenceless field computed from the present algorithm and the auxiliary field respectively. Schematic adapted from Liu <i>et al.</i> (2004)	12
2.3	Schematic of staggered grid. f and g are canonical forms for $((u_y, T)$ and (u_x, u_z, p) respectively. The f and g points are shown as crosses and squares respectively.	18
3.1	Contours of $G_{\text{max}}(\alpha, \beta)$ in the $\alpha - \beta$ plane. α is along the horizontal and β is along the vertical direction. The Reynolds number for each of the three cases corresponds to $\text{Re}=1000$ but the Grashof number in each case is a) $\text{Gr}=0$, b) $\text{Gr}=100$, c) $\text{Gr}=200$. Results computed here are from the same numerical algorithm used in Sameen & Govindarajan (2007)	26
3.2	Curves of $G(t)(\alpha, \beta)$ vs time for the the three cases corresponding to Fig. 3.1 and a value at which the flow is linearly unstable. The Reynolds number for each of the four cases corresponds to $\text{Re}=1000$ but the Grashof number in each case is a) $\text{Gr}=0$, b) $\text{Gr}=100$, c) $\text{Gr}=200$, d) $\text{Gr}=300$. For case a) we have $\beta = 2$ but $\beta = 1.5$ for the rest. $\alpha = 0$ is same for all for cases.	27
3.3	Low (in blue) and high speed (in red) streaks created due to an array of counter-rotating vortices.	29

3.4	Contours of streamwise velocity with the mean subtracted at the time of maximum growth in the $y - z$ plane. Here the z - direction is the horizontal direction. The initial perturbation is the optimal perturbation for $(\alpha = 0, \beta = 2)$ and $Re = 1500, Gr = 0$	30
3.5	Low (in blue) and high temperature (in red) 'streaks' created due to an array of counter-rotating vortices.	31
3.6	Contours of temperature at the time of maximum growth in the $y - z$ plane. Here the z - direction is the horizontal direction. The initial perturbation is the optimal perturbation for $(\alpha = 0, \beta = 2)$ and $Re = 1500, Gr = 200$	31
4.1	Time series of vorticity, Ω_z evolution at a point $y = 1/2$ for $Re = 7000$	34
4.2	Evolution of the normalized disturbance energy, $E(t)/E(0)$ vs time. The Energy here is averaged over one computational box so that the wave component is averaged out. The solid curve is obtained from linear stability and the circles from DNS. Clockwise from top-left, we have $Re = 5000, Re = 7000, Re = 9000$ and $Re = 12000$	35
4.3	Evolution of the normalized disturbance energy, $E(t)/E(0)$ with time for $Re = 7000$. The solid curve is obtained from linear stability and the circles from DNS. Clockwise from top-left, we have $Gr = 2 \times 10^5, Gr = 4 \times 10^5, Gr = 7 \times 10^5$ and $Gr = 10^6$	37
4.4	The envelope of the energy growth (seen as a black solid line) obtained from linear theory for $Re=3000$ is plotted with time. The DNS results corresponding to energy growth of optimals which have a maximum at various times are shown in various colours. The blue curve in particular corresponds to the optimal which attains the maximum energy of all optimals and intersects the envelope at the time when that is achieved.	38
4.5	Evolution of the normalized disturbance energy, $E(t)/E(0)$ with time for $\alpha = 1, \beta = 0$. The solid curve is envelope of the energy evolution and the circles represent the evolution of the optimal disturbance computed from DNS. a) $Re=2000$, b) $Re=3000$, c) $Re=4000$, d) $Re=5000$	39

4.6	Contours of the vertical velocity, u_y at the time when maximum energy is attained at $Re=3000$ for input optimal perturbations from a) linear theory and b) DNS	39
4.7	Same as Fig.4.5 but for a) $Re=3000$ $Gr=1000$, b) $Re=3000$ $Gr=100000$, c) $Re=4000$ $Gr=1000$, b) $Re=4000$ $Gr=100000$	40
4.8	Contours of the vertical velocity, u_y at the time when maximum energy is attained, at $Re=3000$ and $Gr=100000$ for a) linear theory and b) DNS	40
4.9	Contours of the temperature, T at the time when maximum energy is attained, at $Re=3000$ and $Gr=100000$ for a) linear theory and b) DNS	41
4.10	Evolution of the normalized disturbance energy, $E(t)/E(0)$ with time for streamwise vortex, $\alpha = 0, \beta = 2$ The solid curve is envelope of the energy evolution and the circles represent the evolution of the optimal disturbance computed from DNS for $Gr=0$ and a) $Re=300$, b) $Re=500$, c) $Re=1000$, d) $Re=1500$	42
4.11	Same as Fig. 4.10 but for $Re=1000$ and a) $Gr=200$, b) $Gr=300$	42
5.1	Contours of total streamwise velocity at the time of maximum growth in the $y - z$ plane. Here $y-$ is along the vertical direction and $z-$ along the horizontal. The initial perturbation is the optimal perturbation for $(\alpha = 0, \beta = 2)$ and $Re = 1000, Gr = 0$	45
5.2	Evolution of the normalized disturbance energy, $E(t)/E(0)$ with time for the optimal disturbance at $Re=1000$ and $(\alpha = 0, \beta = 2)$. The red crosses indicate the times at which the flow contours are plotted later in the chapter	45
5.3	Contours of the streamwise velocity with the mean subtracted at $t=24$, in the $y - z$ plane, $x=L_x/2$ with the $z-$ direction being along the horizontal. Here $Re=1000$ and $Gr=0$	46
5.4	Contours of the streamwise velocity with the mean subtracted at $t=24$, in two $x - z$ planes given by $y=L_y/2$ (left) and $y=L_y/6$ (right). The $x-$ direction is along the horizontal. Here $Re=1000$ and $Gr=0$	47
5.5	Same as Fig. 5.3 but at $t=67$	48
5.6	Same as Fig. 5.4 but at $t=67$	48
5.7	Same as Fig. 5.3 but at $t=93.6$	49

5.8	Same as Fig. 5.4 but at $t=93.6$	49
5.9	Same as Fig. 5.3 but at $t=156$	50
5.10	Same as Fig. 5.4 but at $t=156$	51
5.11	Same as Fig. 5.3 but at $t=240$	52
5.12	Same as Fig. 5.4 but at $t=240$	52
5.13	Contours of the streamwise velocity with the mean subtracted at $t=24$, in the $y-z$ plane, $x=L_x/2$ with the z - direction being along the horizontal. Here $Re=1000$ and $Gr=200$	53
5.14	Contours of the streamwise velocity with the mean subtracted at $t=24$, in two $x-z$ planes given by $y=L_y/2$ (left) and $y=L_y/6$ (right). The x - direction is along the horizontal. Here $Re=1000$ and $Gr=200$	54
5.15	Same as 5.13 but at $t=67$	54
5.16	Same as 5.14 but at $t=67$	55
5.17	Same as 5.13 but at $t=93$	55
5.18	Same as 5.14 but at $t=93$	56
5.19	Same as 5.13 but at $t=156$	56
5.20	Same as 5.14 but at $t=156$	57
5.21	Same as 5.13 but at $t=240$	57
5.22	Same as 5.14 but at $t=240$	58
5.23	Evolution of the normalized disturbance energy, $E(t)/E(0)$ with time for the optimal disturbance at $Re=1000$ and $Gr=200$ ($\alpha = 0, \beta = 2$). The red, green and black curves show the evolution of the potential energy, total energy and kinetic energy respectively. The blue curve is the kinetic energy evolution for the unstratified case and has already been plotted in Fig. 5.2	58
5.24	Contours of the temperature, T in the (left) $x-z$ plane at $y=L_y/2$ and (right) in the $y-z$ plane. The horizontal direction in the left and right figure is the x - and z - direction respectively. Here $t=24$	61
5.25	Same as Fig. 5.24. But at $t=67$	61
5.26	Same as Fig. 5.24. But at $t=93$	62
5.27	Same as Fig. 5.24. But at $t=156$	62
5.28	Same as Fig. 5.24. But at $t=240$	63

List of Tables

- | | | |
|-----|--|----|
| 4.1 | Comparison of complex frequency w obtained from DNS and linear theory corresponding to the curves in Fig. 4.2. The grid parameters are $Nx = 17$, $Ny = 71$, $\gamma = 2.0$ | 36 |
| 4.2 | Comparison of complex frequency w obtained from DNS and linear theory corresponding to the curves in Fig. 4.7 for $Re = 7000$ and $Pr = 1$. The grid parameters are $Nx = 17$, $Ny = 101$, $\gamma = 2.0$ | 36 |

Contents

Abstract	vii
List of Figures	xii
List of Tables	xiii
1 Introduction	1
2 Direct Numerical Simulation : Method	7
2.1 Stratified Channel flow	7
2.2 Time Stepping algorithm and accuracy	10
2.3 Choice of solution methodology	10
2.4 The Pressure-velocity projection method	11
2.5 Spatial discretization and accuracy	14
2.6 Staggered grid and grid stretching	17
3 Transient growth : linear theory	21
3.1 Linear stability theory	21
3.2 Transient Growth	24
3.3 The Lift up mechanism	28
4 Direct Numerical Simulation : Validation	33
4.1 Evolution of the most unstable mode	33
4.2 Transient Growth	36
5 Three dimensional streak breakdown and transition	43
5.1 The basic streak instability	43

6 Conclusions and future outlook	65
References	67

CHAPTER 1

INTRODUCTION

The mechanisms underlying transition from laminar to turbulent flow have been intensely studied over the past few decades. Considerable progress has been made on many fronts though a coherent picture still remains elusive. Understanding this transition process from a physical and mathematical perspective is of course dependent on the nature of the flow situation. The simplest and the oldest approach for shear flows is based on first order perturbation theory, referred to as linear stability theory (Orr, 1907). The approach involves perturbing an existing flow situation whose stability has to be ascertained (termed the base flow) and subsequently linearizing the governing equations in the perturbed field. This linearization procedure tacitly assumes that the imposed perturbation is in effect infinitesimal or from a physical point of view, arbitrarily small. The linearized equations in the perturbation are then analyzed and the solutions examined. The existence of solutions which grow exponentially in time proves the flow to be unstable to arbitrarily small perturbations but the lack of such solutions says little about the actual stability of the flow. This method is also referred to as modal analysis since one only considers the behaviour of the most unstable mode and assumes that the behaviour of the flow is governed by the same. Studying the linear stability has seen considerable success in understanding and predicting the initial instability process in various flow problems but has fallen woefully short in others. The Rayleigh-Benard (RB) instability (Chandrasekhar, 1961) which occurs when fluid between two walls is heated from the bottom is a prime example where the former is true. Linear theory predicts the critical Rayleigh number of instability as well as the wavelength of the same. The predictions from linear stability in this case match extremely well with experimental observations. But there remain fluid flow problems in simple geometries where the predictions of linear theory seem to have little or no relation to what is actually observed. An example of this is a class of shear flows, notably Poiseuille or Hagen-Poiseuille flow in a channel or pipe driven by an external pressure gradient and Couette flow generated by two parallel walls or concentric cylinders moving in opposite directions. In case of plane channel flow

the Reynolds number at which transition from laminar to turbulent flow occurs in reality is less than half of that predicted by linear theory (Re_L) (Nishioka *et al.*, 1975). Cylindrical pipe flow and couette flow fare rather worse since linear theory predicts that they are *stable* for all Re something that is well removed from what is observed (Coles, 1965).

Another paradigm in understanding transition is the global non-linear stability theory (Joseph, 1976). This approach, as in the previous case, examines the evolution of an imposed perturbation over an existing base flow. But in variance with linear stability theory the perturbation equations are not linearized. In general the response of a particular physical system to externally imposed perturbations would depend on the value of the physical parameters involved (which can be quantified by relevant non-dimensional numbers). The aim of global stability theory is to find the range of values of the relevant non-dimensional numbers where the energy of any externally imposed disturbance, having *arbitrary* size and structure, decays *monotonically* at all times. This approach is in some sense the other extreme to linear stability theory in terms of analysis of transition. The latter can only treat infinitesimal disturbances while the former is valid for disturbances having arbitrarily large amplitudes. The surprising aspect however is that for the case of Rayleigh-Benard flow, the first instability predicted by linear analysis occurs at precisely that Rayleigh number where an arbitrary perturbation ceases to decay monotonically as predicted by the global theory. The same is not however true for the aforementioned class of shear flows where the Reynolds (Re_ε) number corresponding to global stability is much smaller than the linear instability case. Also here, Re_ε is much less than the experimentally observed transition Reynolds number which in turn is much less than that predicted by linear theory, as stated previously.

Other methods have therefore been devised to explain this observed discrepancy notably the secondary instability mechanism (Herbert, 1983) and the recently espoused dynamical systems methods which look for full non-linear solutions of the governing equations (Hamilton *et al.* (1995); Jimenez & Pinelli (1999); Waleffe (1995*a,b*)). In the case of shear flows, the latter methodology involves treating the governing equations as a dynamical system in the flow field, with the Reynolds number being the control parameter. Here laminar and turbulent flow are characterized by the existence of a laminar attracting state (which is stable below a

particular value of Re) and a ‘turbulent attractor’ which they find, exists only after a particular value of the Re . They find the turbulent attractor to be a class of exact travelling-wave solutions of the Navier-Stokes equation which are shown to represent a saddle point in phase space. This approach therefore states that the possibility of transition to turbulence exists only when the Reynolds number reaches the value when the turbulent attractor begins to exist. This theory has enjoyed success both in terms of experimental verification (Hof *et al.*, 2004) and in predicting the correct range of Reynolds numbers for transition (Kerswell, 2005). In spite of the success of this theory however, it does not attempt to predict the actual transition mechanism but defines the conditions necessary for it. Further, this theory cannot in fact explain the earlier mentioned discrepancy related to the difference in behaviour of Rayleigh-Benard flow on one hand and shear flows on the other.

A key contribution that was made in explaining the difference in behaviour of the two class of problems was by Chimonas (1979) who did an inviscid analysis of a shear flow problem and considered not just the traditional modal analysis but the contribution from the whole spectrum of the linear operator. He found the existence of algebraically growing disturbances which are asymptotically stable but can cause growth in short time intervals. Landahl (1980) clarified this mechanism further using an elegant and simpler analysis. In a series of papers by Butler & Farrell (1992); Farrell (1988) and Reddy & Henningson (1993, 1994) who considered the full (*i.e.* with viscosity included) linearized equations, it was shown that this transient growth of disturbances is due to the non-normality of the Linear operator. Trefethen *et al.* (1993) in a seminal paper showed while the behaviour of normal operators is described purely by their eigenvalues, it is not so for non-normal operators. They were also able to show that the energy of flow field whose evolution is described by a normal linear operator monotonically decays at all times if the flow is linearly stable (*i.e.* from the perspective of modal analysis). The linear operator which governs the evolution of disturbances in Rayleigh-Benard convection can in fact be shown to be normal. This explains the nature of transition here and the fact that below the linear stability limit, the energy of *all* disturbances decay monotonically and the linear analysis is sufficient to predict the first transition. The linear operators for the case of shear flows mentioned above are however *non-normal* which means that even when the eigenfunctions are all stable (*i.e.* below

the linear instability limit), one can have transient growth of disturbance energy. This implies that if this transient growth is sufficiently large, it can trigger transition through the non-linear terms that had been excluded in the linear theory. The key aspects of the transient or nonmodal growth have been studied from various perspectives. Trefethen *et al.* (1993) showed the relationship of the maximum growth to the nature of the pseudospectra of the linear operator and the quantitative results were computed by Reddy & Henningson (1993). The pseudospectrum of a linear operator refers to the spectrum of the operator when it is given a small perturbation by another arbitrary linear operator, the magnitude of this perturbation being the parameter that defines the pseudospectrum. Reddy & Henningson (1993) also obtained the conditions for no transient growth and showed that they matched with the results from the global analysis of Joseph (1976).

The interaction of shear with buoyancy and heat transfer, essentially the problem being studied here, is a frequently occurring problem in the atmosphere and the oceans. An important physical phenomenon which involves this interaction is in the formation and sustenance of a convective storm. Wilhelmson & Klemp (1981) study such storms and the role of both aspects. They find that, though convection is the dominant source of energy initially, the presence of vertical wind shear is crucial for the stability and sustenance of such storms (also studied by Browning & Ludlam (1962)). Further, Weisman & Klemp (1982) found that vertical wind shear also plays a crucial role in the splitting of such storms (referred to as Supercells) into left and right moving storms. The problem also has relevance in flows in the earth's interior, notably in the liquid outer core and the magma. However the driving mechanism which generates the shear in this case is the earth's rotation (called Ekman pumping) and frequently involves massive viscosity variations ($\sim 10^6$).

Therefore understanding the dynamics of this interaction process is of considerable physical interest. Studies on channel flows involving unstable stratification have been numerous and are based on a variants of modal stability analysis. Gallagher and Mercer (1964) and Gage & Reid (1968) used linear theory to study unstably stratified Couette flow and Poiseuille flow respectively. Lipps (1971) investigated the problem using two-dimensional numerical simulations at high Richardson numbers. After the onset of convection and in the presence of weak shear, the convection rolls can either be aligned with the flow (longitudinal rolls) or transverse to it. Various authors have studied the problem of the pattern selection of the rolls

using weakly non-linear theory and the Ginzburg-Landau equation. They find that for weak imposed shear, transverse rolls dominate initially only to make way for longitudinal rolls as the shear increases in intensity. Carriere & Monkewitz (1999) have attempted to understand this change in the roll-type in terms of a convective to absolute instability transition.

The flow regime we consider here is different from the ones mentioned previously in that we have a channel flow with a strong shear and weak imposed stratification. In the previous regime described, the flow is convection dominated and hence we expect that modal analysis would be sufficient for describing the dynamics. But since nonmodal growth has been shown to be important to describe some types of shear flow, we specifically focus on this aspect here. The case of shear flow subject to a weak imposed *stable* stratification has been considered by Farrell & Ioannou (1993) who used the inviscid equations only. Bakas *et al.* (2001) extended this analysis to include viscosity and studied the evolution of the dominant structures in the flow from the transient growth results. A recent study by Biau & Bottaro (2004) has also looked at transient growth in stably stratified couette flow. All the mentioned authors find that the presence of stable stratification reduces the maximum transient growth. The case of *unstable* stratified channel flow was examined in a recent paper by Sameen & Govindarajan (2007) where the effect of viscosity stratification was also considered. Their results indicate some surprising trends in the nature of the transient growth mechanism in the presence of buoyancy, especially when the heat diffusivity is large. The differences pertain both to the magnitude of the transient growth and the nature in which it manifests. In the absence of unstable stratification, the maximum growth occurs for disturbances which are streamwise independent, a result that hardly changes with imposed stable stratification (see (Biau & Bottaro, 2004) and (Schmid & Henningson, 2001)). With an unstable density profile however added however, Sameen & Govindarajan (2007) find that the maximum growth is observed for disturbances which are spanwise independent and the growth rates are an order of magnitude higher.

The present endeavour aims to study this problem through Direct Numerical Simulations, which are full solutions of the Navier-Stokes equation. We initially verify many of the results stated in Sameen & Govindarajan (2007) through DNS for very small disturbances. We then consider larger disturbances which might be capable of triggering transition through nonmodal growth and trace the physical

mechanism of this transition in both two and three dimensions. The thesis is organized as follows : The second chapter focuses on details of the numerical method and the various related issues like algorithmic complexity and order of accuracy in space and time. The third chapter is a brief summary of results in transient growth considered in this thesis and also considers the lift-up mechanism for the case of stratified flows. In the fourth chapter we present detailed benchmarks for the numerical implementation which validate its physical output for the problem in question. In the final chapter, we present and compare the results for the non-linear transition mechanism in three dimensions, with and without stratification.

CHAPTER 2

DIRECT NUMERICAL SIMULATION : METHOD

The channel flow problem has been among the most well studied problems using Direct Numerical Simulations primarily because of the symmetries present and the consequent simplification of the formulation. In this chapter we describe in detail the numerical approach and approximations used alongwith the spatio-temporal accuracy of the methods used.

2.1 Stratified Channel flow

The schematic of the flow in question is shown in Figure 2.1 It is generated by driving a fluid between two parallel plates with a constant external pressure gradient. The walls of the fluid are maintained at constant, but different, temperatures such that the lower wall is hotter. The theoretical laminar flow solution is a parabolic profile in the streamwise velocity while the mean temperature is a linearly decreasing profile from the hot to the cold wall. The latter is obtained under the assumptions that the viscosity is independent of the temperature and that the Boussinesq approximation is valid. The streamwise, spanwise and wall-normal directions are along the x , z and y axes. The flow field is characterised by the velocity, temperature and the pressure fields (u, v, w, p, T, T_m) , the temperature field T here representing the deviation from the mean background conduction profile, T_m . The Boussinesq approximation requires that $T(x, y, z, t) \ll T_m(y)$ which means that the deviation of the temperature field caused by advection is much smaller than the local conduction profile. The governing equations consist of the Navier-Stokes equation under the Boussinesq approximation (Eq. 2.4) under which the velocity field remains divergenceless (Eq. 2.6) . The temperature evolves in time according to an advection diffusion equation (Eq. 2.5) . The imposed boundary conditions are the no-slip condition for the velocity field (condition 2.13) on the walls while the temperature deviation, T vanishes at the walls (condition 2.14) under the assumption that the walls are maintained at a constant total temperature. Periodic

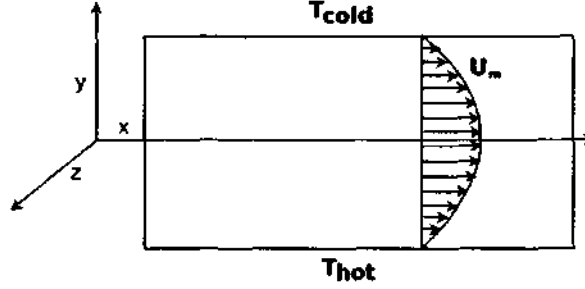


Figure 2.1: Schematic of a stratified channel flow.

boundary conditions are imposed in the streamwise and spanwise directions for all the fields (condition 2.10), the periods in the respective directions being L_x and L_z . The governing equations are :

$$\frac{\partial \mathbf{u}}{\partial t} + \mathbf{u} \cdot \nabla \mathbf{u} = -\frac{\nabla p}{\rho_0} + g\alpha T \mathbf{j} + \nu \nabla^2 \mathbf{u} + \frac{p_m}{\rho_0} \mathbf{i} \quad (2.1)$$

$$\frac{\partial T}{\partial t} + \mathbf{u} \cdot \nabla T = v \frac{\Delta T}{2d} + \kappa \nabla^2 T \quad (2.2)$$

$$\nabla \cdot \mathbf{u} = 0 \quad (2.3)$$

Here $\mathbf{u} \equiv (u, v, w)$ is the three-dimensional velocity field defined along (x, y, z) , p_m is the imposed constant pressure gradient along the x direction and ρ_0 is the density of the background mean flow at the center of the channel. ν , κ and α are the kinematic viscosity, heat conductivity and coefficient of thermal expansion of the fluid and are assumed to be independent of the temperature. Further, g represents the acceleration due to gravity and ΔT , the total temperature difference between the two walls, so that $\Delta T = T_m(0) - T_m(2d)$. The variables are non-dimensionalised as follows :

$$\mathbf{u}' = \mathbf{u}/U_c, \quad (x', y', z') = (x/d, y/d, z/d), \quad t' = t/(U_c/d)$$

$$T' = T/\Delta T, \quad p' = p/\rho_0 U_c^2$$

Here, U_c is the center-line velocity and d the channel half-width. After rewriting the governing equations in the non-dimensional variables and dropping the primes,

we obtain the equations in the following form :

$$\frac{\partial \mathbf{u}}{\partial t} + \mathbf{u} \cdot \nabla \mathbf{u} = -\nabla p + \frac{Ra}{Re^2 Pr} T \mathbf{j} + \frac{1}{Re} \nabla^2 \mathbf{u} + (2/Re) \mathbf{i} \quad (2.4)$$

$$\frac{\partial T}{\partial t} + \mathbf{u} \cdot \nabla T = \nu/2 + \frac{1}{Re \cdot Pr} \nabla^2 T \quad (2.5)$$

$$\nabla \cdot \mathbf{u} = 0 \quad (2.6)$$

$$(2.7)$$

the non-dimensional numbers here are defined as :

$$\text{Reynolds number, } Re = \frac{U_c d}{\nu} \quad (2.8)$$

$$\text{Rayleigh number, } Ra = \frac{g \alpha \Delta T d^3}{\nu \kappa}$$

$$\text{Prandtl number, } Pr = \frac{\nu}{\kappa}$$

Two other non-dimensional numbers which we use frequently in the course of the present discourse and are derived from the above definitions, are :

$$\text{Grashof number, } Gr = \frac{Ra}{Pr} \quad (2.9)$$

$$\text{Richardson number, } Ri = \frac{Ra}{Re^2 Pr}$$

The associated boundary conditions are :

$$\mathbf{u}(x + L_x, y, z + L_z, t) = \mathbf{u}(x, y, z, t) \quad (2.10)$$

$$p(x + L_x, y, z + L_z, t) = p(x, y, z, t) \quad (2.11)$$

$$T(x + L_x, y, z + L_z, t) = T(x, y, z, t) \quad (2.12)$$

$$\mathbf{u}(x, 0, z, t) = \mathbf{u}(x, 2, z, t) = 0 \quad (2.13)$$

$$T(x, 0, z, t) = T(x, 2, z, t) = 0 \quad (2.14)$$

2.2 Time Stepping algorithm and accuracy

The time stepping algorithm used here is a Crank-Nicholson Adam-Bashforth (CN-AB) semi-implicit scheme. This method has a second order accuracy in time. This scheme is elucidated below for the general advection diffusion equation since the equations 2.4-2.14 are variants of this :

$$\frac{\partial f}{\partial t} + \mathbf{u} \cdot \nabla f = \alpha \nabla^2 f \quad (2.15)$$

The presence of the nonlinear advective terms entails their explicit treatment while the diffusive term can be treated in implicit fashion. The implicit treatment of the diffusive term is necessary to improve the numerical stability of the discretized equations as explicit treatments require the use extremely of small time steps. The advective terms are treated using a second order accurate Adam-Bashforth scheme. So that we write :

$$\frac{f^{n+1} - f^n}{\Delta t} = -(\mathbf{u} \cdot \nabla f)^{n+\frac{1}{2}} + \frac{\alpha \nabla^2}{2} (f^{n+1} + f^n) \quad (2.16)$$

the first term on the right hand side is rewritten by noting that according to the Adam Bashforth method, $g^{n+\frac{1}{2}} = \frac{3}{2}g^n - \frac{1}{2}g^{n-1} + O(\Delta t^3)$. Substituting this and rearranging the terms to separate the n^{th} and $n+1^{th}$ iterates we get :

$$(1 - \frac{\alpha \Delta t}{2} \nabla^2) f^{n+1} = -\Delta t (\frac{3}{2} (\mathbf{u} \cdot \nabla f)^n - \frac{1}{2} (\mathbf{u} \cdot \nabla f)^{n-1}) + (1 + \frac{\alpha \Delta t}{2} \nabla^2) f^n \quad (2.17)$$

Now since the RHS of the above equation depends only on the previous iterates which are known one needs to solve a helmholtz equation which can be done by suitably discretizing the Laplacian as is explained in the next section. The Crank-Nicholson scheme is second order accurate also which means the semi-implicit solution Eq. 2.17 is a second order accurate solution of Eq. 2.16.

2.3 Choice of solution methodology

In order to arrive at the approach for solving the set of equations, it is sufficient to consider the case of $Ra = 0$. The principal difficulty in solving Eq. 2.4 with the imposed constraint, 2.6, lies in the nature of the velocity-pressure coupling. The

velocity field has an evolution equation, 2.4 and also has all its boundary conditions specified, unlike the pressure term whose boundary conditions on the walls are unknown. There is however an additional condition imposed on the velocity field, namely 2.6, which one hopes can be used in some form to either eliminate the pressure or obtain boundary conditions for the same. There are different methods that one might take in order to resolve this issue. One is to introduce another variable, in the form of the vorticity which is defined as $\omega = \nabla \times \mathbf{u}$. The pressure is clearly eliminated from the equations when their curl is taken (since $\nabla \times \nabla p = 0$) but at the cost of introducing another variable whose boundary conditions are unknown and must still be determined. Following this approach leads us to the so called vorticity-velocity ($\omega - \mathbf{u}$) formulation or a vorticity-vector potential ($\omega - \Psi$) formulation where another variable is introduced at the cost of the velocity ($\mathbf{u} = \nabla \times \Psi$).

The method adopted here solves the equations 2.4-2.14 in their existing form (commonly referred to as the ‘primitive-variables’ formulation) without introducing the vorticity or vector-potential. Working in this paradigm, there are two directions that one can proceed in. The first approach involves *using* the zero-divergence criterion, 2.6, to derive the boundary conditions for the pressure and then solve the equations since now the BCs of all the field variables are known. This approach, first used by Kleiser & Schumann (1980) is called the Influence-Matrix approach and is loosely based on decomposing the field variables into homogenous and particular solutions of the governing equations. The second technique considers the elimination of the pressure term as a projection of the velocity on the space of divergenceless fields. The technique that we here use is a variant of a velocity projection technique and is explained in detail in the next section. The primary reason for its choice is the simplicity of the method over the Influence Matrix formulation and ease of implementation of the boundary conditions.

2.4 The Pressure-velocity projection method

The first implementation of this approach is due to Chorin (1968) who treated the pressure term merely as a Lagrange multiplier to enforce the continuity equation on the velocity. Using an operator splitting approach, he obtained a two-step predictor-corrector method where the velocity evolution equation is decoupled from

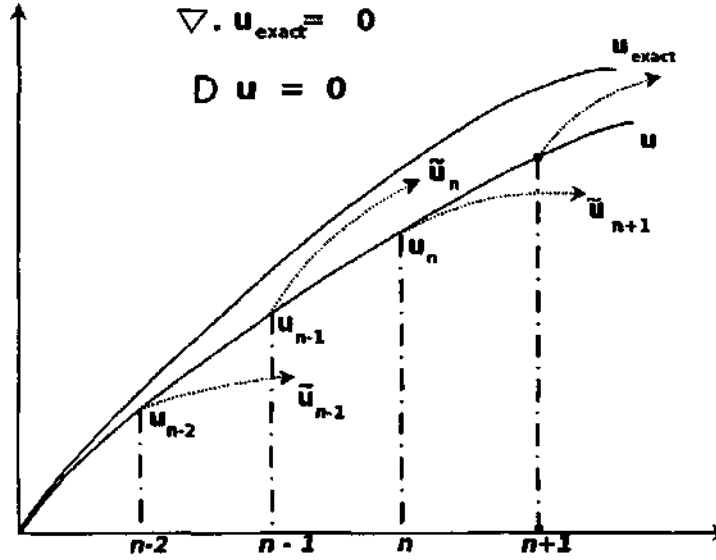


Figure 2.2: Schematic of the projection method the evolution of the velocity field with time. u_{exact} , u and \tilde{u} are the exact velocity field (*i.e.* the solution of the continuous system, the divergenceless field computed from the present algorithm and the auxiliary field respectively. Schematic adapted from Liu *et al.* (2004)

the pressure. In the first step, an auxiliary velocity field is evolved as per the Navier-Stokes equation but with the pressure term absent. The subsequent step involves projecting this auxiliary velocity field onto the space of non-divergent vector fields to obtain the corrected velocity field satisfying the continuity equation. This approach is clearly shown in the schematic 2.2 where u_{exact} , u and \tilde{u} are the exact velocity field (*i.e.* the solution of the continuous system, the divergenceless field computed from the present algorithm and the auxiliary field respectively. We derive the projection in a series of steps the starting point being the Navier-Stokes equation written in the following time-discretized form

$$\frac{(u^{n+1} - u^n)}{\Delta t} = -\nabla p^{n+1} + (-u \cdot \nabla u)^{n+\frac{1}{2}} + \frac{1}{2Re} \nabla^2 (u^{n+1} + u^n) \quad (2.18)$$

Writing the LHS as :

$$\text{LHS} \equiv \frac{(u^{n+1} - \tilde{u}^{n+1} + \tilde{u}^{n+1} - u^n)}{\Delta t} = \frac{(u^{n+1} - \tilde{u}^{n+1})}{\Delta t} + \frac{(\tilde{u}^{n+1} - u^n)}{\Delta t} \quad (2.19)$$

We now choose to define $\tilde{\mathbf{u}}^{n+1}$ as :

$$\frac{(\mathbf{u}^{n+1} - \tilde{\mathbf{u}}^{n+1})}{\Delta t} = -\nabla p^{n+1} \quad (2.20)$$

Eq. 2.18 now becomes,

$$\frac{(\tilde{\mathbf{u}}^{n+1} - \mathbf{u}^n)}{\Delta t} = (-\mathbf{u} \cdot \nabla \mathbf{u})^{n+\frac{1}{2}} + \frac{1}{2Re} \nabla^2 (\mathbf{u}^{n+1} + \mathbf{u}^n) \quad (2.21)$$

Eqs. 2.20 and 2.21 constitute the exact projection method. This is not however solvable as the RHS of 2.21 contains a \mathbf{u}^{n+1} term. Eliminating this using 2.20 we get,

$$\frac{(\tilde{\mathbf{u}}^{n+1} - \mathbf{u}^n)}{\Delta t} = (-\mathbf{u} \cdot \nabla \mathbf{u})^{n+\frac{1}{2}} + \frac{1}{2Re} \nabla^2 (\tilde{\mathbf{u}}^{n+1} + \mathbf{u}^n) - \frac{\Delta t}{2Re} \nabla^2 (\nabla p) \quad (2.22)$$

Therefore we get :

$$(\tilde{\mathbf{u}}^{n+1} - \mathbf{u}^n) = \Delta t (-\mathbf{u} \cdot \nabla \mathbf{u})^{n+\frac{1}{2}} + \frac{\Delta t}{2Re} \nabla^2 (\tilde{\mathbf{u}}^{n+1} + \mathbf{u}^n) + O(\Delta t^2) \quad (2.23)$$

2.20 and 2.23 constitute the basic projection method due to Chorin. The problem occurs in applying the boundary conditions for pressure. Chorin (1968) used Neumann boundary conditions for the pressure but that has been shown to give $O(1)$ error in the pressure by Liu *et al.* (2004). Kim & Moin (1985) improved the above approach by using an auxilliary pressure variable to improve the boundary conditions and the time accuracy of the method. In the approach of Kim & Moin (1985) however, the boundary conditions of the auxilliary pressure variable, ϕ are not homogenous. A slight modification in their method is introduced wherein ϕ from the previous time is now introduced in the momentum equation. This modified method for the case for $Re=0$, as stated in Lee *et al.* (2001) is specified below

$$\frac{\tilde{\mathbf{u}}^{n+1} - \mathbf{u}^n}{\Delta t} = -\nabla \phi^n + (-\mathbf{u} \cdot \nabla \mathbf{u})^{n+\frac{1}{2}} + \frac{1}{2Re} \nabla^2 (\tilde{\mathbf{u}}^{n+1} + \mathbf{u}^n) \quad (2.24)$$

$$\mathbf{u}^{n+1} - \tilde{\mathbf{u}}^{n+1} = -\Delta t (\nabla \phi^{n+1} - \nabla \phi^n) \quad (2.25)$$

$$\nabla \cdot \mathbf{u}^{n+1} = 0 \quad (2.26)$$

$$\nabla^2 (\phi^{n+1} - \phi^n) = \nabla \cdot \tilde{\mathbf{u}}^{n+1} \quad (2.27)$$

$$\nabla p = \nabla \phi^{n+1} - \frac{\Delta t}{2Re} \nabla(\nabla^2(\phi^{n+1} - \phi^n)) \quad (2.28)$$

It is seen from the above equations that the splitting method naturally affects the temporal accuracy of the numerical approach as in the case of 2.23. This accuracy for the set of equations 2.24-2.28 can be easily estimated essentially using the same approach as in Eq. 2.23 since :

$$\mathbf{u}_{\text{exact}} - \mathbf{u} = \frac{\Delta t^2}{2Re} \nabla(\nabla^2 p) + O(\Delta t^3) \quad (2.29)$$

Which means that the velocity field has second order error $O(\Delta t^2)$.

2.5 Spatial discretization and accuracy

The spatial discretization procedure is implemented by taking into consideration the nature of the boundary conditions. The domain is periodic in the stream-wise and spanwise directions, making those amenable to representation by fourier series. The vertical direction too can be treated in spectral form by using a Chebyshev collocation method but we treat it using finite differences instead. This mixed-finite difference spectral approach has considerable advantages in terms of the simplicity of the implementation of boundary conditions. The fourier series representation of the field variable is :

$$\mathbf{u}(x, y, z, t) = \sum_{k_x=0}^{N_x} \sum_{k_z=0}^{N_z} \tilde{\mathbf{u}}(k_x, y, k_z, t) e^{i(k_x x + k_z z)} \quad (2.30)$$

$$p(x, y, z, t) = \sum_{k_x=0}^{N_x} \sum_{k_z=0}^{N_z} \tilde{p}(k_x, y, k_z, t) e^{i(k_x x + k_z z)} \quad (2.31)$$

$$T(x, y, z, t) = \sum_{k_x=0}^{N_x} \sum_{k_z=0}^{N_z} \tilde{T}(k_x, y, k_z, t) e^{i(k_x x + k_z z)} \quad (2.32)$$

The transformation allows us to re-write the equations 2.4 - 2.6 in terms of the variables $(\tilde{\mathbf{u}}, \tilde{p}, \tilde{T})$ in (k_x, y, k_z) space. It is easy to see that the derivatives in x- and z- directions have the following simple representations in k -space :

$$\frac{\partial}{\partial x} \rightarrow ik_x \quad \frac{\partial}{\partial z} \rightarrow ik_z \quad (2.33)$$

$$\frac{\partial^2}{\partial x^2} \rightarrow -k_x^2 \quad \frac{\partial^2}{\partial z^2} \rightarrow -k_z^2 \quad (2.34)$$

$$\nabla \rightarrow i(j\frac{\partial}{\partial y} + ik_x + kk_z) \quad (2.35)$$

$$\nabla^2 \rightarrow (\frac{\partial^2}{\partial y^2} - k_x^2 - k_z^2) \quad (2.36)$$

The nonlinear terms by virtue of being product terms can be expressed as a convolution

$$f.g \rightarrow \sum_{k_x} \sum_{k'_x} \sum_{k_z} \sum_{k'_z} \bar{f}(k_x, y, k_z) \cdot \bar{g}(k'_x, y, k'_z) \quad (2.37)$$

$$k_x + k'_x = N_x \quad k_z + k'_z = N_z$$

Direct summation of this term has a algorithmic complexity of $O(N_x^2 N_z^2)$ which is prohibitively expensive. A pseudospectral approach due to Orszag(1977) can be used to reduce the complexity to a vastly more efficient $O(N_x N_z \log(N_x N_z))$. This is done by taking recourse to the efficient Fast Fourier transform methods which are used here from the open source FFTW library. But the pseudospectral method suffers from the so-called aliasing error which occurs because of product terms coming from the higher wave numbers. This can be removed by the ubiquitous Orszag 3/2 rule.

The derivatives along the y -axis are evaluated using finite-differences which are based on taylor-explansions about each grid point. However y - derivatives occuring in different terms of the equations 2.4 - 2.6 are in general, expressed in terms of different finite-difference formulas. In the advective-diffusive equation, Eq. 2.16 for example, the second derivative terms are expressed using a second order accurate, central difference scheme shown below :

$$\frac{\partial^2 f}{\partial y^2} \Big|_j = \frac{f_{i-1} - 2f_i + f_{i+1}}{\Delta y^2} + O(\Delta y^3) \quad (2.38)$$

The first derivative terms occuring in the nonlinear terms (having the form $f \frac{\partial g}{\partial y}$) are expressed using a 6th order accurate central difference (CD_6) scheme in the interior of the domain. The point just next to the wall is expressed using a second order central difference (CD_2) formula while the next point is expressed using a

4th order central Difference (CD_4) formula. The stencils for these derivatives are as follows :

$$\left. \frac{\delta^{CD_6} f}{\delta y} \right|_j = \frac{f_{i+3} - 9f_{i+2} + 45f_{i+1} - 45f_{i-1} + 9f_{i-2} - f_{i-3}}{60\Delta y} + O(\Delta y^7) \quad (2.39)$$

$$\left. \frac{\delta^{CD_4} f}{\delta y} \right|_j = \frac{-f_{i+2} + 8f_{i+1} - 8f_{i-1} + f_{i-2}}{12\Delta y} + O(\Delta y^5) \quad (2.40)$$

$$\left. \frac{\delta^{CD_2} f}{\delta y} \right|_j = \frac{f_{i+1} - f_{i-1}}{2\Delta y} + O(\Delta y^3) \quad (2.41)$$

Note that the spatial accuracy of the system as a whole is actually $O(\Delta y^3)$ since that is accuracy of the second derivative terms. So the order of accuracy of the system is not changed if a higher order scheme is used for the nonlinear terms. But in using a higher order scheme for the non-linear terms, one aims not to improve the order of accuracy but the *spectral* resolution. The computation of the non-linear terms by the very nature of the term requires a very high spectral resolution. The spectral resolution of the CD_6 scheme is more than twice that of the CD_2 scheme and this is crucial in the computation of the advection terms even though the overall accuracy of the system is unchanged. The notion of spectral resolution of finite difference schemes has been considered in detail in Chapters 10 and 11 of Sengupta (2004). In particular the author notes, “*It is well known that the spectral method has the best accuracy among all discrete schemes. Hence we will calibrate all other methods with respect to spectral methods...*”. The author goes on to show that the CD_6 scheme has a better spectral resolution than the CD_2 scheme. In fact the compact schemes used in general in literature use high order accurate schemes in the interior and lower order accuracy schemes at the boundary (usually second or third order), as explained in Sengupta (2004) and in Lele (1992). Further in section 11.5 (titled “Order of Approximation vs. Resolution”) of Sengupta (2004), the author states the following, “*The order of approximation usually refers to a local series expansion and is measured by leading truncation error term. However, resolution refers to the ability of numerical schemes to resolve various length scales involved in the problem, and a best view is provided by expressing the unknowns by the Fourier-Laplace transform....*”, and later, “*All these results indicate that the formal accuracy of the the truncation error cannot be the sole criteria. A better depiction would be in the spectral plane.*”. In fact our computation of the growth

rate of the most unstable eigenfunction had an error $\sim 7 - 10\%$ when the CD_4 was used in the interior instead of CD_6 for the cases computed in Chapter 4, Fig. 4.2. The CD_6 scheme however was found to perform better and had an error $\sim 2\%$ as seen in Table 4.1 in Chapter 4.

Another necessary issue to consider is the form of computation of the non-linear terms. The non-linear convolution term can be expressed in three different forms - the advective ($f \frac{\partial g}{\partial y}$), divergence ($\frac{\partial fg}{\partial y}$) or skew-symmetric ($\frac{1}{2}(f \frac{\partial g}{\partial y} + \frac{\partial fg}{\partial y})$) forms. Here we compute the non-linear terms in the advective form because of the simplicity in its computation.

2.6 Staggered grid and grid stretching

On a normal grid system (*i.e.* non-staggered), all field variables are specified at the same set of grid points and so are all the derivatives. The problems however appear in the solution of Poisson equations of the same type as Eq. 2.27. The second derivative of one field variable (here ϕ) equals the first derivative of another field variable (\bar{u}). The same form occurs in solving 2.24 where the second derivative of the \bar{u} equals terms having the first derivative of ϕ . The issue occurs because of the way in which a Poisson equation must be solved. Consider the case when the first derivative is represented by the CD2 scheme in 2.41, so that the second derivative term is written as $\frac{\delta^{CD_2}}{\delta y} (\frac{\delta^{CD_2} f}{\delta y}) = \frac{f_{i+2} - 2f_i + f_{i-2}}{4\Delta y^2}$. A 'canonical' equation of the form mentioned earlier can be written as :

$$\frac{\partial f}{\partial y} = \frac{\partial^2 g}{\partial y^2} \quad (2.42)$$

Writing the discrete form using CD2 as mentioned earlier, we get

$$\frac{g_{i+2} - 2g_i + g_{i-2}}{4\Delta y^2} = \frac{f_{i+1} - f_{i-1}}{2\Delta y} \quad (2.43)$$

It is seen that the LHS and RHS have *no* points in common, the so called even-odd decoupling. The form of Eq. 2.43 means that with reference to the walls, the even and odd points can be separated into two different classes of equations with two different solutions. The solution of the Eq. 2.43 therefore oscillates between these two solutions leading to the well documented pressure oscillations in the primitive

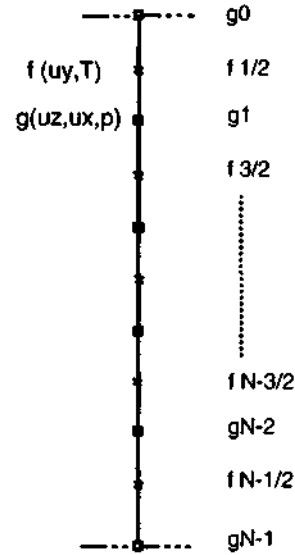


Figure 2.3: Schematic of staggered grid. f and g are canonical forms for $((u_y, T))$ and (u_x, u_z, p) respectively. The f and g points are shown as crosses and squares respectively.

variables formulation on a normal grid.

A way out is the use of a staggered grid where the variables f and g are stored in staggered fashion, as illustrated in Fig. 2.3. We shall refer to the positions of the field variables as 'f-points' and 'g-points' where (u_y, T) lie on the former and (u_x, u_z, p) on the latter as shown in the schematic. The choice of the grid is explained as follows : In case of the equations 2.24 - 2.28, the variables u_x and u_z are related to ϕ not through an equation of the form, 2.42 but of the form $f = \frac{\partial^2 g}{\partial y^2}$, which does not have the even-odd decoupling problem mentioned before. This occurs because the Fourier series method reduces $\nabla\phi$ to $(i(k_x\mathbf{i} + k_y\mathbf{k}) + \frac{\partial}{\partial y}\mathbf{j})\phi$, so it is only u_y which is related to ϕ in the form 2.42, thus explaining the choice of the staggering arrangement. Thus u_x, u_z and ϕ are stored at the same points whereas the u_y term is evaluated at a set of points which is half a grid-step removed.

The discrete version of 2.42 can now be written in similar fashion as 2.43 on the staggered grid. Suppose we evaluate it at a point y_i which is a 'g-point'. Then we define the discrete derivative in CD2 form as $\delta^{CD2} f / \delta y = (f_{i+1/2} - f_{i-1/2}) / \Delta y$. Now the second derivative term for g can be evaluated and we get $(\delta^{2CD2} g) / \delta y^2 =$

$(g_{i+1} - 2g_i + g_{i-1})/\Delta y^2$ so that Eq. 2.42 now becomes :

$$\frac{g_{i+1} - 2g_i + g_{i-1}}{\Delta y^2} = \frac{f_{i+1/2} - f_{i-1/2}}{\Delta y} \quad (2.44)$$

The storage of the temperature field is subject to some debate. Verzicco(2001) for example advocates that the temperature values be stored at the same points as the pressure (ϕ in this case). We find oscillations in the temperature if this is used which can be explained easily. The temperature and the vertical velocity equation (as can be seen from Eqs. 2.4 and 2.5) have an obvious symmetry which seems to imply that they should be treated similarly. We therefore evaluate the temperature terms at the same point as u_y , the vertical velocity.

The momentum equations for u_x , u_z and the pressure poisson equation are therefore evaluated at g-points while the evolution equations for u_y and T are evaluated at the f-points. One last issue that must be addressed is regarding the evaluation of the non-linear terms on this grid. The u_y equation for example needs the u_x and u_z values on the f-points which must therefore be interpolated from the g-points (and *vice - versa* for interpolating the u_y field on the f-points). A 5th order lagrange interpolation is therefore used for this purpose.

Further, the grid in the y - direction is stretched so that it is denser near the walls and rarer near the center of the channel. This is enforced since much of the energy production in both transitional and turbulent shear flows occurs in a layer close to the walls. This is not entirely unexpected considering the high shear regions in the vicinity of the walls. The grid stretching that we employ is given as :

$$y(j) = \frac{2d}{2.0} \left(1 - \frac{\tanh(\gamma(1 - \frac{2j\Delta y}{Ly}))}{\tanh(\gamma)} \right) \quad (2.45)$$

where $j \in [0 : N_y - 1]$ and $y(0) = 0$ and $y(N_y - 1) = 2$. Here γ is the grid stretching parameter, a higher value of which causes denser clustering of grid points near the wall. Therefore to completely define the grid, we need four parameters (N_x, N_y, N_z, γ) in three dimensions and three parameters (N_x, N_y, γ) in two dimensions.

CHAPTER 3

TRANSIENT GROWTH : LINEAR THEORY

The brief precis of the theory of transient growth and the underlying physical mechanism is presented here. The primary emphasis is on the the notion of optimal perturbation and the the ‘lift-up’ effect that causes it, especially in the presence of unstable stratification.

3.1 Linear stability theory

When a perturbation is added to an existing base flow state (not necessarily stable), the equation governing its evolution can be linearized if the perturbation is sufficiently small. Of course an linearization process implies that the perturbation is in-effect infinitesimal (as is frequently referred to in literature) but in certain cases the notion of “sufficiently small” can be quantified from physical considerations, as shall be explained later. The governing equations are, of course the Navier-Stokes equation and the temperature advection-diffusion equations coupled together under the Boussinesq approximation as stated in Eqs. 2.4 - 2.6 .Our starting point is a steady base flow state characterized by a mean parallel profile $U_m(y)$ and the base temperature is assumed to be zero everywhere (note that this is the deviation from the mean temperature under the Boussinesq approximation so the actual base temperature field is the linear conduction profile). We now add an external perturbation given by (u, v, w, T) so that the actual flow field is $(u + U, v, w, T)$. Eqs. 2.4 - 2.6 are then written in these variables and linearized which means that any terms in the above equations non-linear in the perturbation quantities are assumed to be small and ignored. This leads us to :

$$\frac{\partial u}{\partial t} + U \frac{\partial u}{\partial x} + vU' = -\frac{\partial p}{\partial x} + \left(\frac{1}{Re}\right)\nabla^2 u \quad (3.1)$$

$$\frac{\partial v}{\partial t} + U \frac{\partial v}{\partial x} = -\frac{\partial p}{\partial y} + \frac{Ra}{Re^2 Pr} T + \left(\frac{1}{Re}\right)\nabla^2 v \quad (3.2)$$

$$\frac{\partial w}{\partial t} + U \frac{\partial w}{\partial x} = -\frac{\partial p}{\partial z} + \left(\frac{1}{Re}\right) \nabla^2 w \quad (3.3)$$

$$\frac{\partial T}{\partial t} + U \frac{\partial T}{\partial x} - v/2 = \left(\frac{1}{Re.Pr}\right) \nabla^2 T \quad (3.4)$$

Taking the divergence of linearized momentum equations, we get an equation for the pressure given by

$$\nabla^2 p = -2U' \frac{\partial v}{\partial x} + Ri \frac{\partial T}{\partial y} \quad (3.5)$$

This allows us to eliminate the pressure from the v momentum equation by applying the operator ∇^2 to Eq 3.2. We therefore get,

$$\left(\left(\frac{\partial}{\partial t} + U \frac{\partial}{\partial x}\right) \nabla^2 - U'' - \frac{1}{Re} \nabla^4\right) v = Ri \left(\frac{\partial^2}{\partial x^2} + \frac{\partial^2}{\partial y^2}\right) T \quad (3.6)$$

A second equation is required to completely describe the evolution of the flow. This can be obtained in terms of the normal vorticity given by $\eta = \frac{\partial u}{\partial z} - \frac{\partial w}{\partial x}$. This equation is obtained from the u and w momentum equations and we get,

$$\left(\frac{\partial}{\partial t} + U \frac{\partial}{\partial x}\right) \eta = -U' \frac{\partial v}{\partial z} + \frac{1}{Re} \nabla^2 \eta \quad (3.7)$$

The above equation alongwith Eqs 3.6 an 3.4 completely describe the evolution of the perturbation. The fact that the domain is periodic in the x and z directions allows us to use a Fourier representation in those directions similar to the one used in 2.30 - 2.32 and the corresponding formulas for the derivatives stated in Eq 2.33 - 2.36. We thus write the stability equation in normal-mode form, i.e. in terms of individual modes represented by the wavenumbers α and β in the x and z directions respectively. We now write the three equations together in the following form :

$$\begin{pmatrix} k^2 - D^2 & 0 & 0 \\ 0 & 1 & 0 \\ 0 & 0 & 1 \end{pmatrix} \frac{\partial}{\partial t} \begin{pmatrix} v \\ \eta \\ T \end{pmatrix} + \begin{pmatrix} \mathcal{L}_{OS} & 0 & k^2 Ri \\ i\beta U' & \mathcal{L}_{SQ} & 0 \\ -1/2 & 0 & \mathcal{L}_T \end{pmatrix} \begin{pmatrix} v \\ \eta \\ T \end{pmatrix} = 0 \quad (3.8)$$

where $k^2 = \alpha^2 + \beta^2$ and $D \equiv \frac{d}{dy}$. The operators, \mathcal{L}_{OS} and \mathcal{L}_{SQ} are the Orr-

Sommerfeld and Squire operators given by,

$$\mathcal{L}_{OS} = i\alpha U(k^2 - D^2) + i\alpha U'' + \frac{1}{Re}(k^2 - D^2)^2 \quad (3.9)$$

$$\mathcal{L}_{SQ} = i\alpha U + \frac{1}{Re}(k^2 - D^2) \quad (3.10)$$

$$\mathcal{L}_T = i\alpha U + \frac{1}{Re.Pr}(k^2 - D^2) \quad (3.11)$$

Equation 3.8 can be expressed in the simplified form :

$$\mathbf{M} \frac{\partial}{\partial t} \mathbf{q} = \mathbf{B} \mathbf{q} \quad (3.12)$$

$$\implies \frac{\partial}{\partial t} \mathbf{q} = \mathbf{M}^{-1} \mathbf{B} \mathbf{q} = \mathbf{A} \mathbf{q} \quad (3.13)$$

$$(3.14)$$

where $\mathbf{q} \equiv \begin{pmatrix} v \\ \eta \\ T \end{pmatrix}$ and \mathbf{M} and \mathbf{B} are obvious by correspondence with Eq. 3.8.

Under the framework of Linear stability theory, one looks for travelling wave modes, i.e. for any flow variable, $f(\alpha, \beta, t)$, we have $f = \tilde{f} e^{-i\omega t}$ where ω is in general complex. In fact, if $\omega = \omega_r + i\omega_i$ then $e^{-i\omega t} = e^{\omega_i t} e^{-i\omega_r t}$ which implies that the imaginary part, ω_i represents the *growth rate* of this wave and ω_r the angular frequency. Eq. 3.13 now becomes

$$\mathbf{A} \tilde{\mathbf{q}} = -i\omega \tilde{\mathbf{q}} \quad (3.15)$$

This equation constitutes an eigenvalue problem in ω for each wave number pair (α, β) . For the case of channel flow, this equation possesses an infinite number of discrete eigenvalues. Under the traditional modal framework one looks for the eigenvalue having the *maximum* growth rate, ω_i referred to as the most unstable linear mode. If the most unstable mode has $\omega_i > 0$ then the the flow variables would undergo exponential growth for all times in which case we say that the flow is linearly unstable and not otherwise. The exponential growth occurs till the perturbation becomes sufficiently large for the non-linear terms, ignored in this framework, to become important when this theory is no longer valid. For the case of Poiseuille flow, the flow becomes unstable at $Re_{cr} \sim 5772$.

3.2 Transient Growth

The evolution equation 3.13 can be rewritten in terms of the matrix exponential by writing,

$$\mathbf{q}(t) = e^{At}\mathbf{q}(0) \quad (3.16)$$

where $\mathbf{q}(0)$ is the initial perturbation. Linear stability theory assumes that the stability characteristics are determined purely by the most unstable mode and places little significance on the rest of the eigenspectrum. The energy of the disturbance is written as $\mathcal{E} = \|\mathbf{q}\|_E$. The energy of the system is defined as :

$$\mathcal{E} = \frac{1}{2} \int_V (|u|^2 + |v|^2 + |w|^2 + |T|^2) dV \quad (3.17)$$

and in terms of the flow variables (v, η, T) the same expression can be easily rewritten as :

$$\mathcal{E} = \frac{1}{2k^2} \int_V (|Dv|^2 + k^2|v|^2 + |\eta|^2 + k^2|T|^2) dV \quad (3.18)$$

When the matrix A is normal (meaning that all the eigenfunctions of the matrix A are mutually orthogonal), then it has been shown by Farrell & Ioannou (1996) that

$$G(t) = \frac{\|\mathbf{q}(t)\|_E}{\|\mathbf{q}(0)\|_E} \leq e^{2(\omega_i)_{max}t} \quad (3.19)$$

This means that the growth in energy, $G(t)$ experienced by an arbitrary disturbance is bounded above by that of the most unstable mode. So the energy of evolution of any disturbance described by a normal matrix is determined by the most unstable mode. In fact if the flow is linear and the governing matrix, A is normal, Eq. 3.19 implies that the disturbance energy *monotonically* decays. For the problem in question however, it is found that the matrix A is *not* normal and therefore condition 3.19 is not valid. So even if the fastest growing mode is stable, *i.e.* $(\omega_i)_{max} \leq 0$, the energy can experience growth for intermediate times under the purview of linear theory itself. So it is not just the least unstable mode but the entire spectrum which must be considered. The class of initial conditions which give rise to the maximum transient growth at a particular times are called optimal disturbances and the global optimal being the one which gives the maximum energy growth over all times. It is possible to find the envelope of the energy evolution of optimal disturbances which attain a maximum at every time in an interval. For a

given (α, β) , this envelope can be written as

$$\max_{q(:,0) \neq 0} G(t, \alpha, \beta) = \max_{q(:,0) \neq 0} \frac{\|q(:, t)\|_E}{\|q(:, 0)\|_E} \quad (3.20)$$

where $q(\alpha, \beta, t)$ is written as $q(:, t)$. This means that the energy growth is maximised at *each* time and (α, β) over the space of all initial conditions given by $q(\alpha, \beta, 0)$. Variational methods allow us to write this as

$$G(t, \alpha, \beta) = \max_{q(:,0) \neq 0} \frac{\|e^{A(\alpha, \beta)t} q(:, 0)\|_E}{\|q(:, 0)\|_E} = \|e^{A(\alpha, \beta)t}\|_E \quad (3.21)$$

which is precisely the envelope. The envelope $\|e^{A(\alpha, \beta)t}\|_E$ can be computed accurately using a singular value decomposition, the details of which are given in Schmid & Henningson (2001). Particular interest is reserved towards the maximum growth that can occur for a specific value of (α, β) such that

$$G_{max}(\alpha, \beta) = \max_t G(t, \alpha, \beta). \quad (3.22)$$

A good possibility exists that the greater the $G_{max}(\alpha, \beta)$, greater is the possibility of transition. For a particular set of physical parameters in the problem (here Re , Gr and Pr), one can compute the (α, β) value where the G_{max} attains a maximum which we term as the global maximum.

$$G_{max}^g(\alpha, \beta) = \max_{\alpha, \beta} G_{max}(\alpha, \beta). \quad (3.23)$$

For unstratified Poiseuille flow, Reddy & Henningson (1993) have found that the most energetic optimal occurs for $\alpha = 0$ and $\beta = 2.016$. Since $\alpha = 0$, this mode is referred to as the Streamwise Vortex (SV) mode. Here we present results for $G_{max}(\alpha, \beta)$ for the case of unstratified flow and two cases of unstable stratification with Grashof numbers 100 and 200 respectively. The results are shown in Fig. 3.1 a) and have been obtained from the same numerical algorithm used in Sameen (2004). It can be seen clearly in Fig. 3.1 a) that the maximum value of G_{max} occurs for $\alpha = 0, \beta \sim 2$. As the unstable stratification increases we see that the G_{max}^g increases too. Further there seems to be a shift in the value of the β where the global maximum is obtained, that being closer to $\beta = 1.5$ now. We then plot the G vs t curves at the corresponding parameter values and at the α, β location

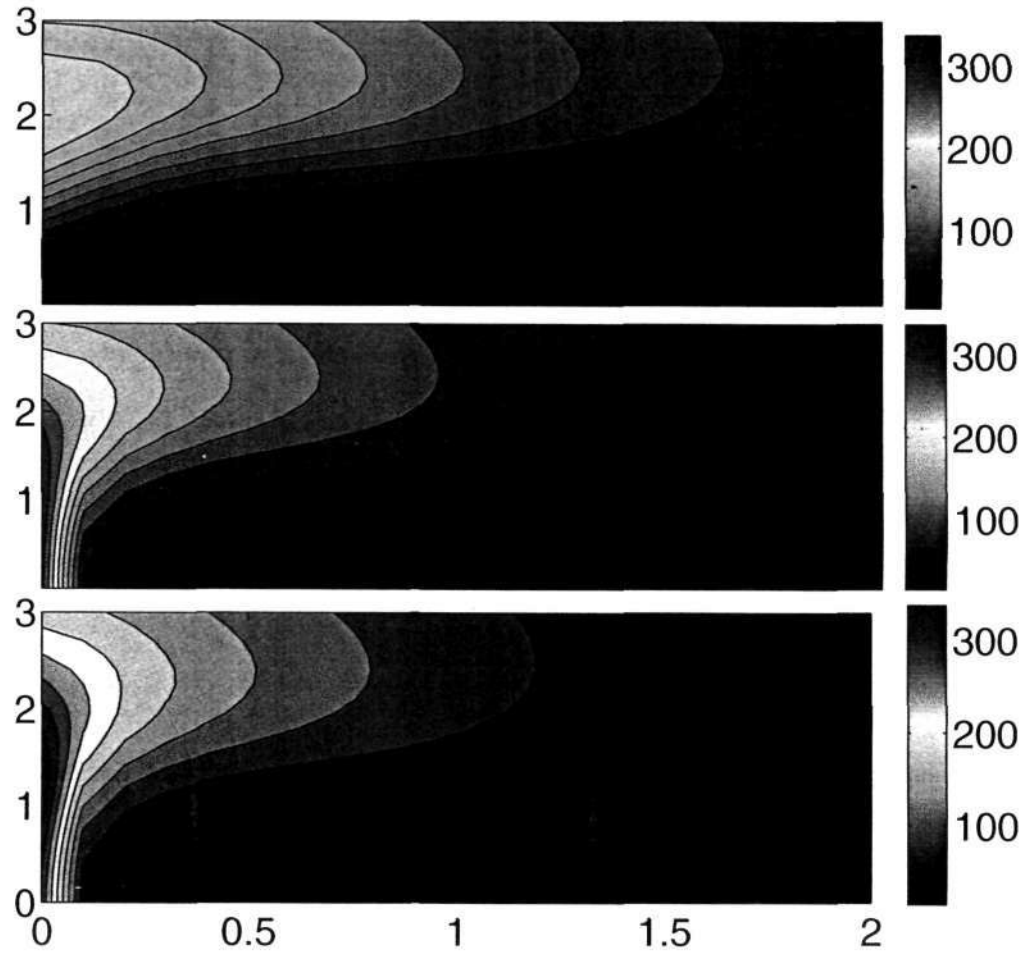


Figure 3.1: Contours of $G_{max}(\alpha, \beta)$ in the $\alpha - \beta$ plane. α is along the horizontal and β is along the vertical direction. The Reynolds number for each of the three cases corresponds to $Re=1000$ but the Grashof number in each case is a) $Gr=0$, b) $Gr=100$, c) $Gr=200$. Results computed here are from the same numerical algorithm used in Sameen & Govindarajan (2007)

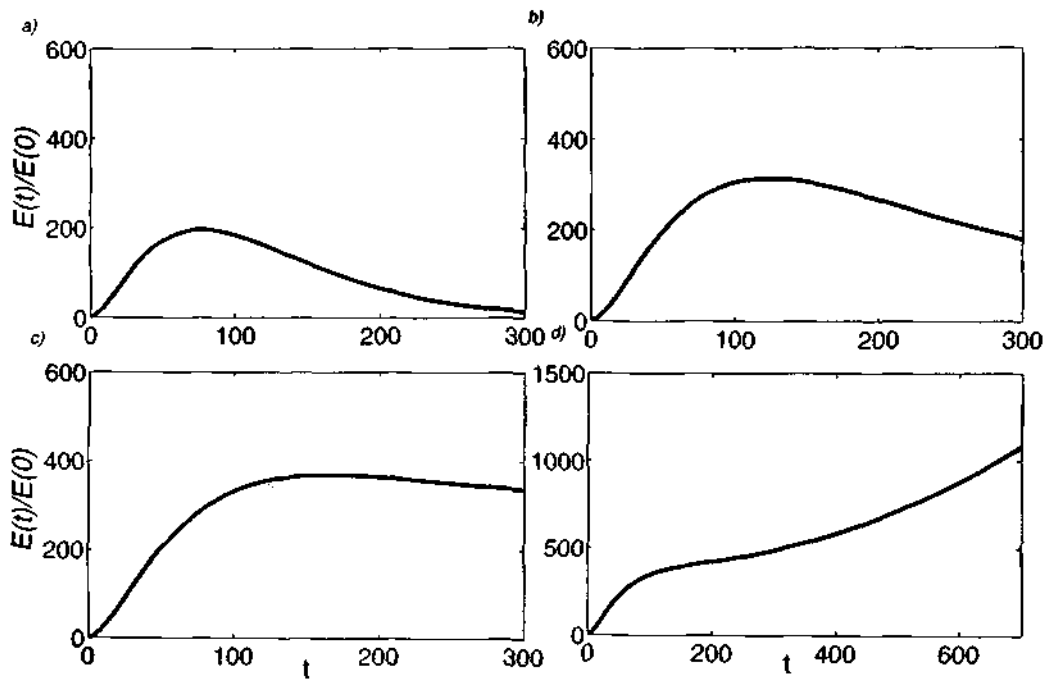


Figure 3.2: Curves of $G(t)(\alpha, \beta)$ vs time for the the three cases corresponding to Fig. 3.1 and a value at which the flow is linearly unstable. The Reynolds number for each of the four cases corresponds to $Re=1000$ but the Grashof number in each case is a) $Gr=0$, b) $Gr=100$, c) $Gr=200$, d) $Gr=300$. For case a) we have $\beta = 2$ but $\beta = 1.5$ for the rest. $\alpha = 0$ is same for all for cases.

where the maximum is attained in each case to see the effect of stratification on the same. It is seen that with increasing stratification, the nature of the growth curves changes considerably as does the maximum value attained which increases. Further, the curve corresponding to $Gr=300$ seems to indicate that the flow might be asymptotically *unstable*. One can understand this by noting that $Gr = 300$ corresponds to $Ra = 2400$ (since $Pr = 1$) in the definition traditionally used in convection literature where the Rayleigh number is based on the total channel width as opposed to the half-width used here. Using the former non-dimensionalisation, the well known result regarding the transition to convection rolls is $Ra_{cr}=1708$ which corresponds to $Ra = 216.2$ here. Even in the presence of shear, studies by Clever & Busse (1991) have shown that the critical Rayleigh number varies only weakly for instability to longitudinal (or streamwise) convection rolls. The case in Fig. 3.2 *d*) therefore indicates the transition to streamwise convective rolls. Once this happens, we do not expect the transient growth mechanism to be of much relevance (something that has been verified through numerical computations, as mentioned later). We therefore confine ourselves to cases where $Ra \leq Ra_{cr}$. Note that variation of viscosity with temperature is not considered here, but it is well known that it can destabilize two-dimensional flow, for example, as seen in Sameen & Govindarajan (2007).

3.3 The Lift up mechanism

The physical reasons as to why transient growth occurs due to the presence of disturbances of the form of streamwise vortices has been well studied in literature. The presence of stratification has not however been considered and this is what we emphasize. We first explain the mechanism for unstratified flow and extend the same to flow with stratification.

We use the aid of a schematic 3.3 to help understand this mechanism. The fig. shows two streamwise vortices aligned in the streamwise direction which is into the paper. The vortices are counter-rotating and advect fluid away from one of the walls and towards the other. Referring to the schematic we see that the vortices advect fluid away from the lower wall towards the channel center. A channel flow has a parabolic mean profile which is slower near the walls and faster near the centerline. Therefore fluid being advected from the lower wall towards the channel

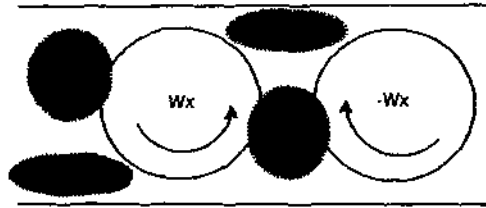


Figure 3.3: Low (in blue) and high speed (in red) streaks created due to an array of counter-rotating vortices.

centerline will have a lower speed than the surrounding fluid. Due to the geometry of the vortices, a well defined region of low speed (relative to the local background mean speed) fluid is formed. This is referred to as a low-speed streak. Similarly high-speed fluid from the center of the channel is advected towards the low mean-speed near the wall creating a localized region of high speed fluid, referred to as a high speed streak. If the parabolic mean profile is subtracted from the total streamwise velocity, the high and low streaks would be visible as regions of positive and negative streamwise velocity respectively. This mean-deducted streamwise velocity is plotted for the an actual computed case corresponding to Fig. 3.2.a) at the time of maximum energy growth in Fig. 3.4. The flow contours shown in Fig 3.4 are computed through the DNS with an initial finite amplitude optimal perturbation with initial energy density $E_v=5 \times 10^{-4}$ at the time of maximum growth. The grid parameters used to compute this contour were $N_x=17$, $N_z=43$, $N_y=78$ and $\gamma=2$ with the dimensions of the domain being $L_x=2\pi$ and $L_z=\pi$ (Note that as a result of non-dimensionalisation, the channel half-width is 1). We see that the streak structure is essentially as expected in the heuristic reasoned argument.

Just as the streamwise vortices redistribute the mean shear to create high and low speed streaks, they also redistribute the mean temperature to create regions of hot and cold 'streaks'. However the difference is that while the mean parabolic profile is symmetric about the centerline, the mean temperature is anti-symmetric. Consider the schematic 3.5, the lower wall is hot and the temperature uniformly decreases till the colder wall. The action of the vortices advects hotter fluid near the wall to the center which is colder. This creates a localized region which is hotter than the surrounding fluid. Further, fluid from the center is advected to the upper wall which is colder. Therefore, another region of localized hot fluid is created near

532.51
p07

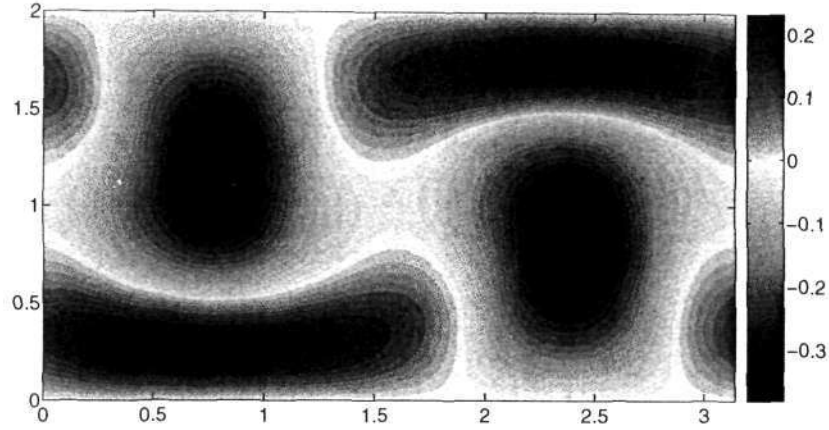


Figure 3.4: Contours of streamwise velocity with the mean subtracted at the time of maximum growth in the $y - z$ plane. Here the z - direction is the horizontal direction. The initial perturbation is the optimal perturbation for $(\alpha = 0, \beta = 2)$ and $Re = 1500, Gr = 0$

the upper wall. Similarly the adjacent pair of coherent vortices advects cold fluid from the top wall to the the bottom wall throughout as shown in the schematic 3.5. The actual temperature contour plot for the evolution of an optimal perturbation at the time of maximum growth is shown at the same Reynolds number but at a Grashof number of 200. Again, the contours agree with the heuristic arguments. The velocity contours at the same time for the stratified case show virtually no difference from the unstratified case. This is because the effect of the temperature on the velocity field is $O(Ri)$ and the Richardson number in the present case is extremely ($Ri = 9 \times 10^{-5}$) small so that the velocity field with stratification present remains largely unchanged.

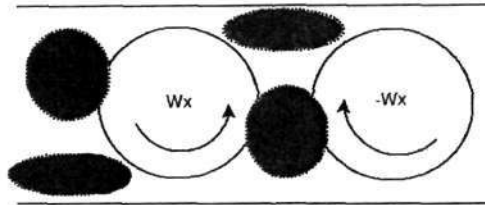


Figure 3.5: Low (in blue) and high temperature (in red) ‘streaks’ created due to an array of counter-rotating vortices.

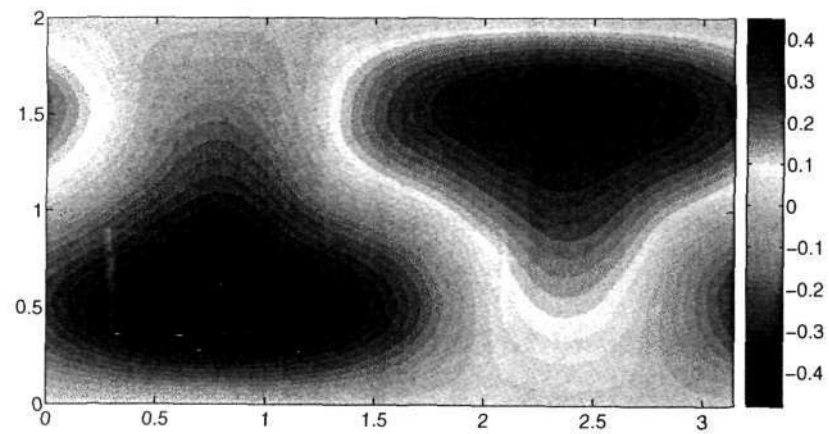


Figure 3.6: Contours of temperature at the time of maximum growth in the $y-z$ plane. Here the z -direction is the horizontal direction. The initial perturbation is the optimal perturbation for $(\alpha = 0, \beta = 2)$ and $Re = 1500, Gr = 200$

CHAPTER 4

DIRECT NUMERICAL SIMULATION : VALIDATION

Any numerical method which hopes to simulate a physical problem must be validated against related experimental and other established numerical results. One speaks of a ‘numerical experiment’ when it is clear that the important length and time scales in the problem have been resolved with sufficient accuracy. In the present chapter, we validate the direct numerical simulation code described in the previous section. The benchmarks that we validate against involve various aspects of stratified and unstratified shear flows in two and three dimensions. The most important benchmark of course corresponds to the phenomenon being studied, namely algebraic growth. Our aim is to study the physics of the nonlinear transition mechanism through this process using DNS but for small imposed disturbances, we expect the results of the DNS to match with that of linear stability theory.

4.1 Evolution of the most unstable mode

Here we consider the evolution of a small disturbance imposed over an existing base flow. The evolution of such a disturbance can be obtained by considering the linearized Navier-Stokes equation, a brief description of which has been given in the first section of Chapter 3. We solve the linearized stability equation given in Chapter 3, Eq. 3.8 in the form of the eigenvalue problem specified in Eq. 3.15. We are in particular interested in the most unstable mode (*i.e.* with the maximum value of ω_i) as is explained in detail in Chapter 3. The approach used here is to obtain the eigenfunctions corresponding to the most unstable mode from the stability equations and consider them as the initial condition for the DNS code. One therefore expects, that for small amplitudes of the input initial disturbance having the structure defined by the most unstable eigenfunction, the nature of the

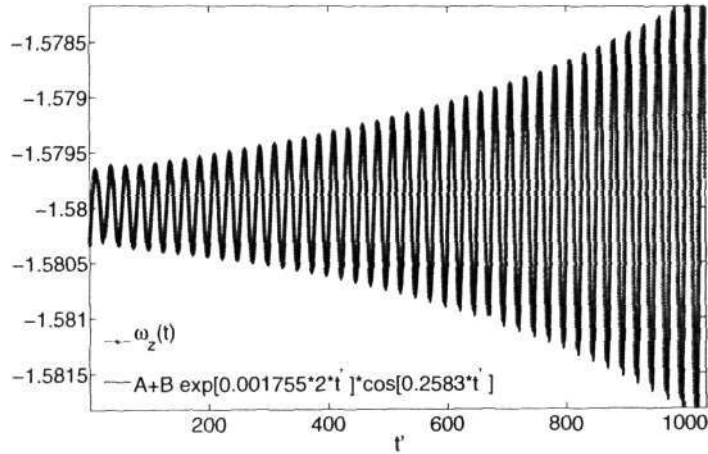


Figure 4.1: Time series of vorticity, Ω_z evolution at a point $y = 1/2$ for $Re = 7000$

evolution of the disturbance is precisely what linear theory predicts. The initial energy density that we use for the input perturbation is $E_v \sim 10^{-12}$. We use the same energy density for all the cases considered in this chapter. Since the evolution of the disturbance in the linear framework is completely characterised by ω_r and ω_i , it suffices to match these numbers obtained from the DNS with the corresponding eigenvalue.

In Fig. 4.1, we plot time series of the vorticity, $\Omega_z(t)$ at $y = 1/2$, $\alpha = 1$ (which is also the value that we use for all the two dimensional computations in this chapter) and $\beta = 0$ (*i.e.* two-dimensional Poiseuille flow). This is superimposed with the expected linear evolution after suitably scaling the amplitude. The figure shows an excellent match between the two curves indicating that the DNS captures the linear evolution (both w_r and w_i) quite well. The grid parameters used here are $N_x = 17$, $N_y = 70$, $\gamma = 2.0$ while the dimensions of the domain are $L_x = 2\pi$ and $L_z = \pi$. The resolution chosen corresponds to the minimum that is required, to get a value of w_i accurate to the fourth decimal place. This choice also seems to ensure that w_r is captured accurately to the second decimal place. We now plot the evolution of the energy of the disturbance integrated over the whole domain with time. The wave component is clearly averaged out and the energy evolves purely according to the growth rate, $2w_i$, the factor of two of course appearing because the energy varies as square of the velocity. The energy evolution obtained from

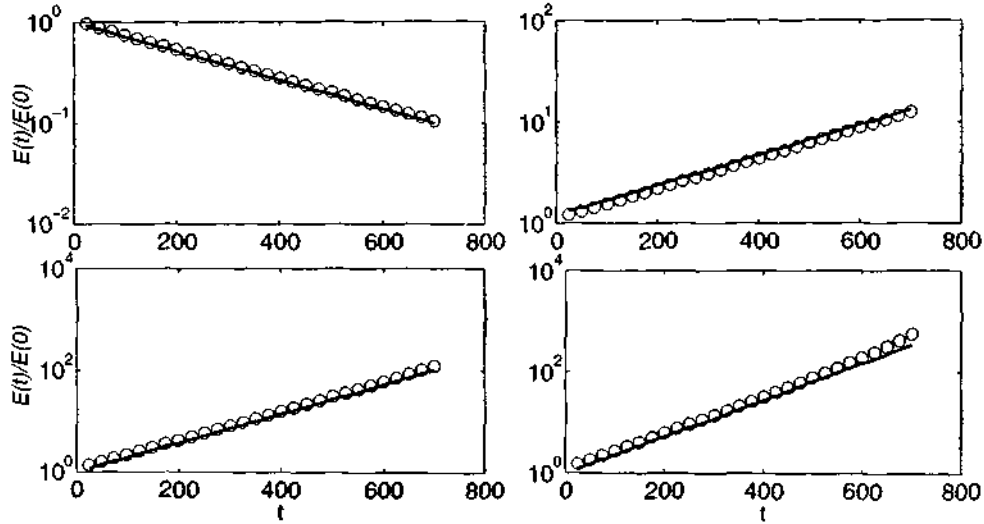


Figure 4.2: Evolution of the normalized disturbance energy, $E(t)/E(0)$ vs time. The Energy here is averaged over one computational box so that the wave component is averaged out. The solid curve is obtained from linear stability and the circles from DNS. Clockwise from top-left, we have $Re = 5000$, $Re = 7000$, $Re = 9000$ and $Re = 12000$

the DNS is plotted against the curve expected from linear theory in Fig. 4.2 for four different Reynolds numbers, 5000, 7000, 9000 and 12000, the grid parameters being the same as in the previous results. In each case, one finds the match to be comparable to that obtained by Rai & Moin (1991). The latter authors do not provide quantitative comparisons and merely show energy evolution curves similar to the one in 4.2 and we find that our results compare favourably.

The w_r and w_i values for the cases described in 4.2 are tabulated in Table 4.1. These values are obtained from a time series plot, similar to the one in Fig. 4.1. The method used to compute these values first involves finding the envelope of the time series plot which corresponds to the exponentially growing part of the wave. This can be found by plotting the energy averaged over a computational box (as in Fig. 4.2). The growth rate is obtained from the energy curve (which is of course a straight line in a semilog graph) and then the original time series is divided throughout by the exponential part, leaving just the wave component whose frequency can be obtained from a standard curve fitting tool (in our case we have

Re	(w_r, w_i) from DNS	(w_r, w_i) from linear analysis
5000	(0.2652, -0.001723)	(0.261, -0.0017)
7000	(0.2583, 0.001755)	(0.255, 0.0017)
9000	(0.2417, 0.003342)	(0.242, 0.0033)
12000	(0.2313, 0.004192)	(0.222, 0.0041)

Table 4.1: Comparison of complex frequency w obtained from DNS and linear theory corresponding to the curves in Fig. 4.2. The grid parameters are $N_x = 17$, $N_y = 71$, $\gamma = 2.0$

Gr	(w_r, w_i) from DNS	(w_r, w_i) from linear analysis
200000	(0.2578, 0.002012)	(0.253, 0.0020)
400000	(0.2513, 0.002363)	(0.256, 0.0023)
700000	(0.2497, 0.002839)	(0.251, 0.0028)
1000000	(0.2524, 0.003321)	(0.257, 0.0033)

Table 4.2: Comparison of complex frequency w obtained from DNS and linear theory corresponding to the curves in Fig. 4.7 for $Re = 7000$ and $Pr = 1$. The grid parameters are $N_x = 17$, $N_y = 101$, $\gamma = 2.0$

used MATLAB). Of course since our aim is to study unstably stratified channel flow, we need to repeat the previous results with stratification added. However the presence of stratification only seems to marginally affect the linear stability results in the Reynolds number regime which we consider in our present study, unless the stratification is large. We therefore consider four cases with fixed Reynolds number ($Re = 7000$) and increasing Grashof numbers, $Gr = 2 \times 10^5$, 4×10^5 , 7×10^5 and 10^6 . Note that the aforementioned parameter values are not in the range that we consider presently but are considered purely for the purpose of code validation. The grid parameters used for the stratified case are $N_x = 17$, $N_y = 91$ and $\gamma = 1.5$. The reason for the need in increased resolution seems to be the complex spatial structure of the temperature eigenfunction. Lesser resolution in the wall-normal direction seems to be insufficient to capture the value of w_i accurately to the fourth decimal place.

4.2 Transient Growth

In this section we consider the evolution of class of disturbances which decay asymptotically in time but can grow for finite intervals of time. This transient growth is a

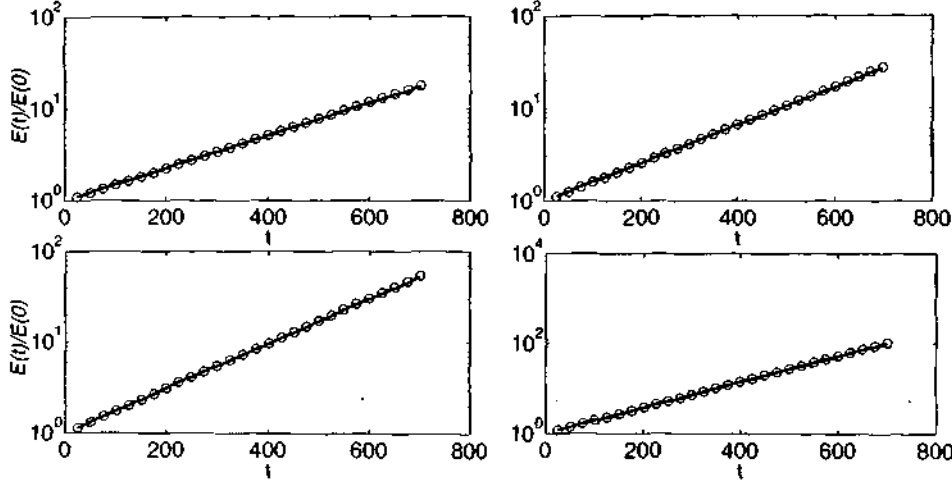


Figure 4.3: Evolution of the normalized disturbance energy, $E(t)/E(0)$ with time for $Re = 7000$. The solid curve is obtained from linear stability and the circles from DNS. Clockwise from top-left, we have $Gr = 2 \times 10^5$, $Gr = 4 \times 10^5$, $Gr = 7 \times 10^5$ and $Gr = 10^6$

linear mechanism and is possible due to the non-normality of the Orr-Sommerfeld and Squire equations as has been explained in Chapter 3. Our starting point is the computation of the optimal perturbations for different wavenumber pairs (α, β) and values of the Reynolds and Grashof numbers. Similarly as described in the previous chapter, the envelope of the evolution of optimal disturbances at different times is computed easily using the singular value decomposition. The benchmarks in the present chapter are established by initializing the DNS with the optimal disturbances and comparing the energy evolution with that obtained from linear theory. Here we study two-dimensional ($\beta = 0$) optimals and the optimal perturbations corresponding to streamwise vortices ($\alpha \neq 0$). The streamwise vortex modes are important because they exhibit the maximal global transient growth (i.e. over (α, β) space) as shown in Chapter 3, Fig. 3.1.

First we consider the evolution of energy for 2D-optimals which achieve a maximum at various times and compare them with the maximal envelope obtained from linear theory. We do this, as mentioned above, for the case $\alpha = 1$, $\beta = 0$ and $Re=3000$. It can be clearly seen from Fig. 4.4, that the growth rate curves obtained from the DNS are in good agreement with the envelope obtained from

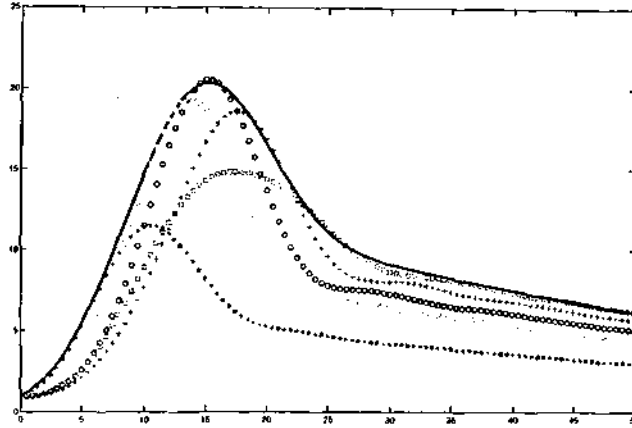


Figure 4.4: The envelope of the energy growth (seen as a black solid line) obtained from linear theory for $Re=3000$ is plotted with time. The DNS results corresponding to energy growth of optimals which have a maximum at various times are shown in various colours. The blue curve in particular corresponds to the optimal which attains the maximum energy of all optimals and intersects the envelope at the time when that is achieved.

linear theory. A similar result has been obtained for other Reynolds numbers. The grid parameters used for the computations in Fig. 4.4 are $N_x = 17$, $N_y = 80$ and $\gamma = 2.0$. This resolution is the minimum needed for ensuring that the maximum energy is accurate to the last significant digit.

Next we consider comparisons between the energy envelope and the evolution of the optimal perturbation at different subcritical Reynolds numbers. Of course the maxima of both curves must coincide and that's clearly seen in Fig. 4.5. More information is obtained by comparing the velocity field at the optimal time obtained from the DNS with the same from linear theory. This is shown in figure 4.6 where we find that the even the associated phase is captured quite accurately.

The corresponding results are shown for stratified flow for two different Reynolds numbers and Grashof numbers. The energy maxima are again computed accurately by the DNS as are the flow fields, indicated by the figures, 4.8 displaying the vertical velocity and, 4.9 the temperature field at the time of maximum energy growth.

The evolution of three dimensional optimal perturbations is computed next for the case $\alpha = 0$ and $\beta = 2$ again for the case of stratified and unstratified flow. Four

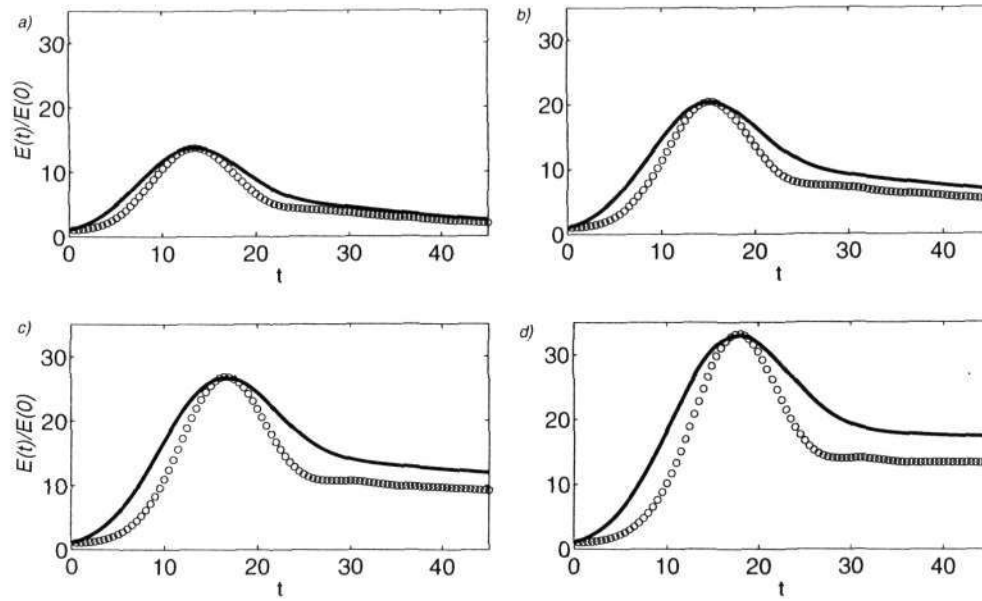


Figure 4.5: Evolution of the normalized disturbance energy, $E(t)/E(0)$ with time for $\alpha = 1$, $\beta = 0$. The solid curve is envelope of the energy evolution and the circles represent the evolution of the optimal disturbance computed from DNS. *a)* $Re=2000$, *b)* $Re=3000$, *c)* $Re=4000$, *d)* $Re=5000$

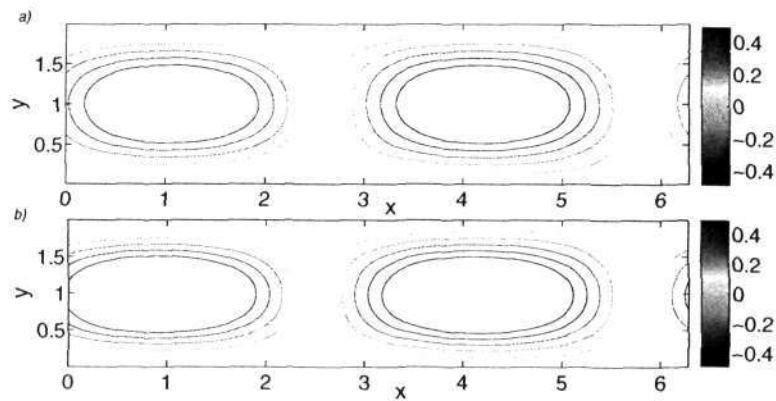


Figure 4.6: Contours of the vertical velocity, u_y at the time when maximum energy is attained at $Re=3000$ for input optimal perturbations from *a)* linear theory and *b)* DNS

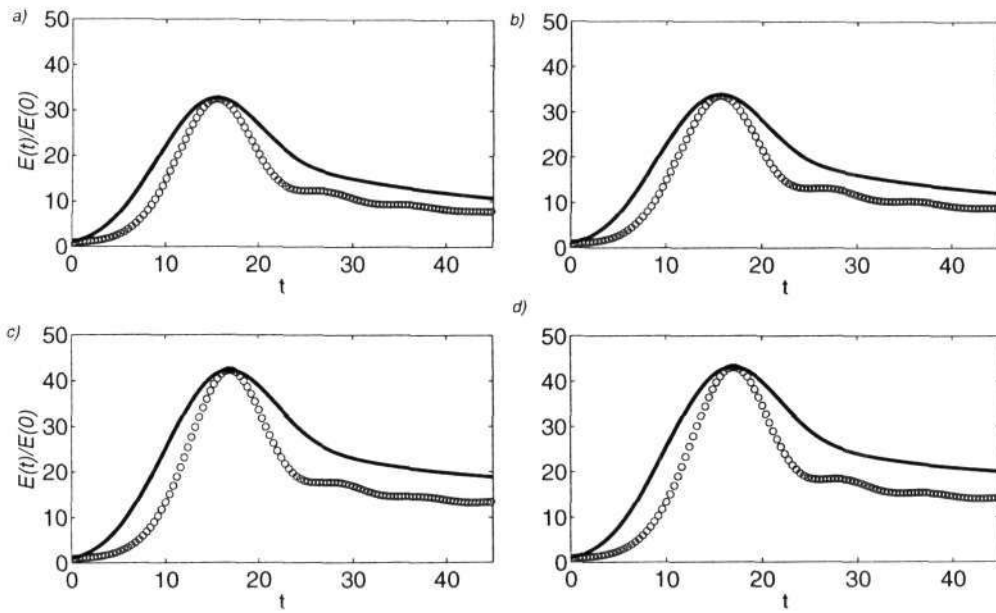


Figure 4.7: Same as Fig.4.5 but for a) $Re=3000$ $Gr=1000$, b) $Re=3000$ $Gr=100000$, c) $Re=4000$ $Gr=1000$, b) $Re=4000$ $Gr=100000$

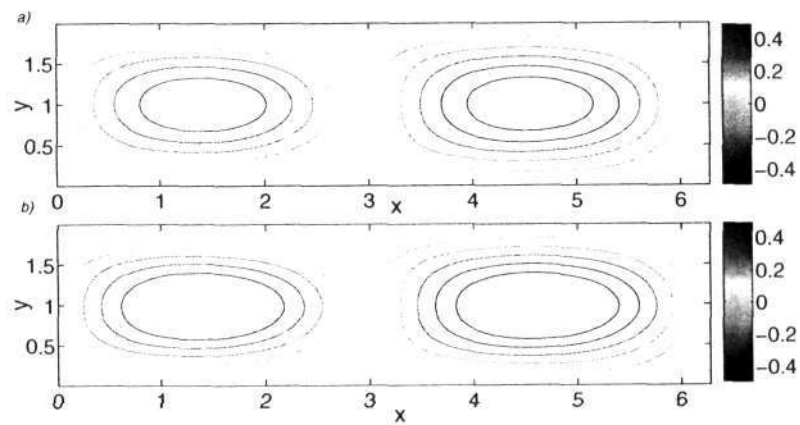


Figure 4.8: Contours of the vertical velocity, u_y at the time when maximum energy is attained, at $Re=3000$ and $Gr=100000$ for a) linear theory and b) DNS

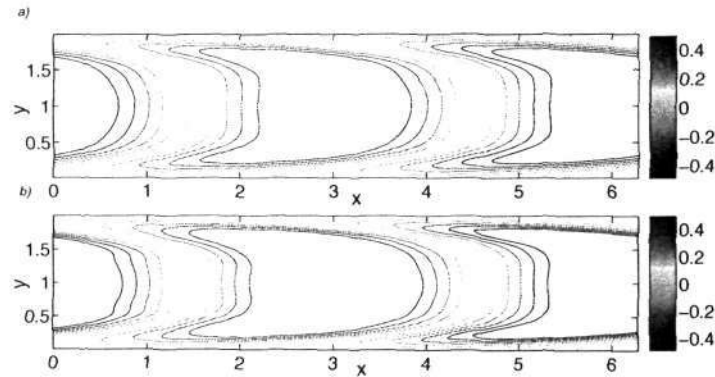


Figure 4.9: Contours of the temperature, T at the time when maximum energy is attained, at $Re=3000$ and $Gr=100000$ for *a)* linear theory and *b)* DNS

different Reynolds numbers between 300 and 1500 are used but in the stratified case, only two cases are computed due to the long computational times involved. The grid parameters used here are $N_x=17$, $N_y=80$, $N_z=43$ and $\gamma=2.0$. From Fig. 4.10 corresponding to the unstratified case and Fig. 4.11 the stratified, we see there is an excellent match in the envelope and the evolution of the optimal disturbance. It is not clear to us why this must be and we have found no studies in literature which have remarked that the evolution of the optimal streamwise vortices is also the envelope for that value of (α, β) . This is an interesting observation that can be further explored though it is not done here.

It has thus been shown that the flow captures the linear evolution of the optimal perturbations accurately and this allows us to proceed to study the non-linear evolution of finite-amplitude optimal perturbations for the cases with and without stratification in the next chapter.

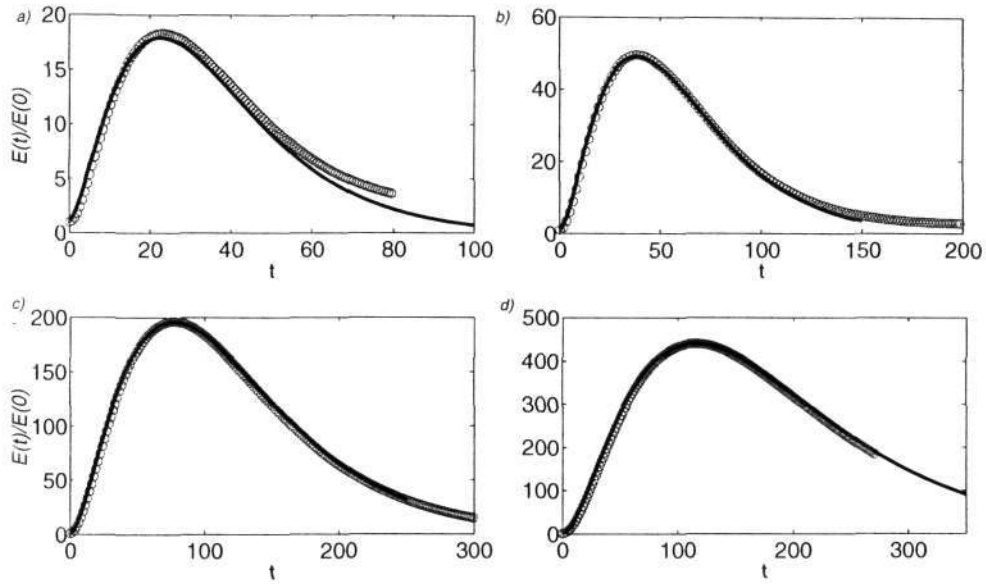


Figure 4.10: Evolution of the normalized disturbance energy, $E(t)/E(0)$ with time for streamwise vortex, $\alpha = 0$, $\beta = 2$. The solid curve is envelope of the energy evolution and the circles represent the evolution of the optimal disturbance computed from DNS for $Gr=0$ and a) $Re=300$, b) $Re=500$, c) $Re=1000$, d) $Re=1500$

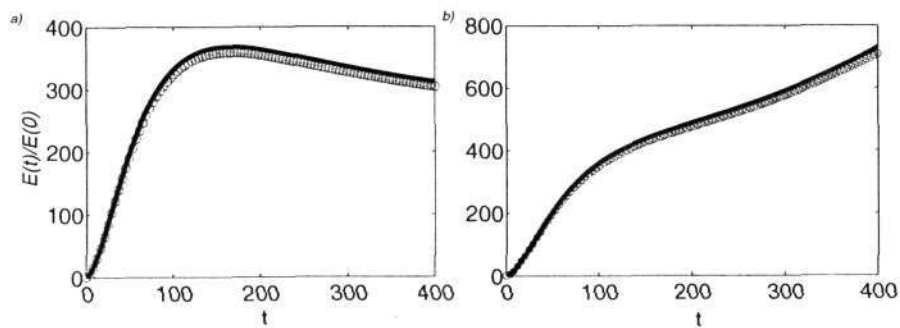


Figure 4.11: Same as Fig. 4.10 but for $Re=1000$ and a) $Gr=200$, b) $Gr=300$

CHAPTER 5

THREE DIMENSIONAL STREAK BREAKDOWN AND TRANSITION

In the present chapter we consider the evolution of finite amplitude optimal disturbances. The latter are of course obtained from linear theory as explained in Chapter 3. It is shown that the flow seeded with optimal disturbances having sufficiently large amplitudes becomes unstable to background noise and transition occurs. This transition process is studied for the flow with and without unstable stratification. Results are compared and the effect of stratification is examined in detail for sub-critical Reynolds and Grashof numbers.

5.1 The basic streak instability

In chapter 3, the formation of streaks was discussed to be a result of redistribution of the mean shear by streamwise vortices. This redistribution of the mean shear causes a distortion of the streamwise velocity and leaves open the possibility of the streak-distorted profile becoming unstable to background noise. Unlike in the case of Chapter 4, Fig. 4.10 the amplitude of the input streak is finite. Depending on the initial amplitude of the optimal disturbance, the maximum energy growth that occurs might be less than that expected from linear theory due to non-linear saturation. Non-linear saturation of the input disturbance generally implies that the disturbance amplitude at the time is comparable to that of the mean flow. Generally a minimum initial amplitude of the streamwise vortex is required to create the conditions for streak breakdown and transition to occur. The threshold amplitude required for transition was investigated in considerable detail by Reddy *et al.* (1998) using a combination of DNS and linear stability of the mean flow distorted by the streaks. These authors using extensive numerical simulations computed the threshold amplitudes for Couette and Poiseuille flow over a wide range of Reynolds numbers. In the present study we keep the amplitude of the

initial optimal perturbations at about twice the threshold amplitude stated in the paper of Reddy *et al.* (1998). This essentially allows for earlier saturation and consequently, reduced computation times. Further we do not attempt to study the effect of stratification on the amplitude threshold due to lack of sufficient time and computational resources. We first illustrate the basic streak instability for $Re=1000$, which corresponds to the lowest Reynolds number at which transition to turbulence is observed in channels. This is lower than the lowest Reynolds number considered by Reddy *et al.* (1998) who start from $Re=1500$. We then consider the effect of unstable stratification on the flow at $Re=1000$ as well as for $Re=1500$.

For $Re=1000$, we start the flow with a finite amplitude disturbance having an energy density of 5×10^{-3} . Note that this is much larger than the value 10^{-12} used in the previous chapter. By knowing the threshold at $Re=1500$ from Reddy *et al.* (1998) and using the scaling $Re^{-1.6}$ that the authors observe from simulations for the threshold amplitude, we find that the energy density used for our computations is about 2.5 times the threshold at $Re=1000$. Further, background noise having an energy density of 10^{-10} in the form of random noise is added to the system. Reddy *et al.* (1998) state that in the absence of this background noise, no transition is observed, mirroring our own computations. Fig 5.1 shows contours of the total streamwise velocity at the time of maximum growth. This mean velocity field is shown to be linearly unstable by Reddy *et al.* (1998). This instability is referred to as streak breakdown and is what we shall examine. The evolution of the energy with time normalized by the initial disturbance energy is plotted in Fig. 5.2.

We now plot the details of the flow field, in particular the streamwise velocity at various times with reference to Fig. 5.2. The first maxima corresponds to the maximum energy growth due to the streak formation process. $t=67$ seems to correspond to the start of the streak instability and there is energy growth after that possibly due to streak breakdown though the disturbance energy eventually decays indicating that the streak instability process has not in fact triggered transition to turbulence at this Reynolds number. Detailed analysis of flow field can help better understand the instability process. The contour plots of the mean-subtracted flow streamwise velocity are plotted below at five different times across one $y - z$ plane and two different $x - z$ planes (one at the center and one near the wall) to enable visualization of both the high-speed and low-speed streaks. The times at which the flow contour plots are shown are marked as crosses in the energy evolution curve

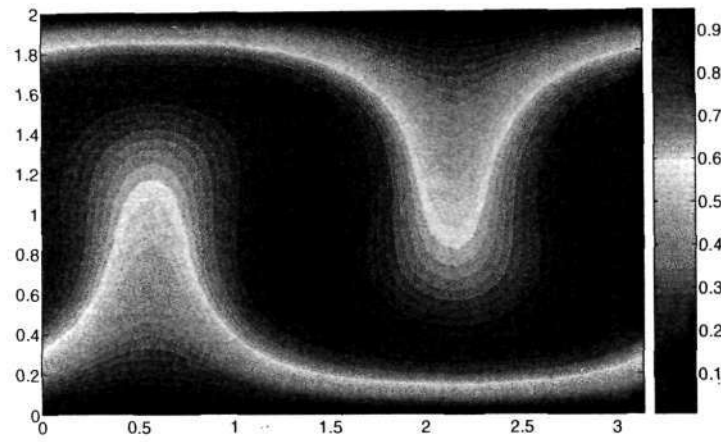


Figure 5.1: Contours of total streamwise velocity at the time of maximum growth in the $y - z$ plane. Here y - is along the vertical direction and z - along the horizontal. The initial perturbation is the optimal perturbation for $(\alpha = 0, \beta = 2)$ and $Re = 1000, Gr = 0$

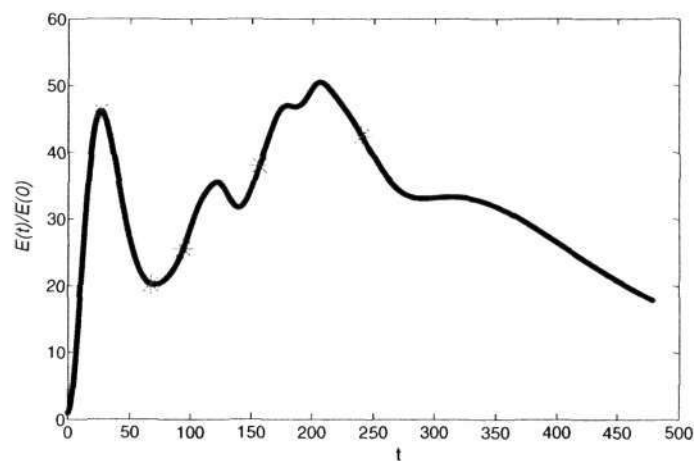


Figure 5.2: Evolution of the normalized disturbance energy, $E(t)/E(0)$ with time for the optimal disturbance at $Re=1000$ and $(\alpha = 0, \beta = 2)$. The red crosses indicate the times at which the flow contours are plotted later in the chapter

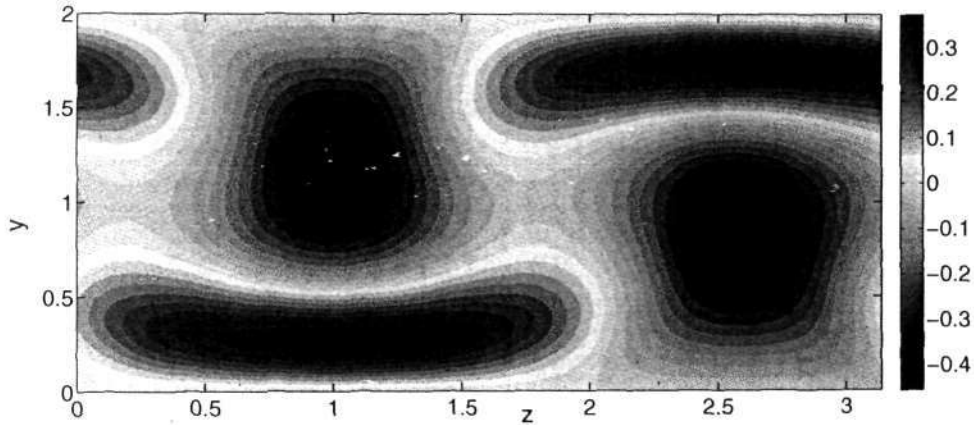


Figure 5.3: Contours of the streamwise velocity with the mean subtracted at $t=24$, in the $y-z$ plane, $x=L_x/2$ with the z - direction being along the horizontal. Here $Re=1000$ and $Gr=0$

shown in Fig. 5.2. We now examine the evolution of the input disturbance using the flow contour plots. Figs. 5.3 and 5.4 are the optimal disturbances at the time of maximum growth attained by the lift-up process explained in Chapter 3 and it is clear that no instability has occurred yet.

The $Re=1000$ case undergoes streak breakdown and transition but the disturbances soon decay to the laminar state.

In fact the instability does not begin until $t=67$ where the flow field is plotted in Fig. 5.5 and 5.6. The waviness of both the low-speed and high-speed streaks heralds the start of an instability. This is corroborated by the fact that the energy of evolution of the disturbance, shown in Fig.5.2 has a turning point implying that the instability just starts to draw energy from the mean shear. After the first turning point in Fig. 5.2 at $t=67$, the energy grows in two different legs, first increasing then a small decrease and another large increase to the maximum after which the energy starts decaying. The contour plots help understand the physical reasons for the existence of these two legs. Fig.5.7 and 5.8 show the streamwise velocity contours at $t=93$, which is well in the middle of the first leg. Here we find that though the waviness in the low-speed streaks near the center has changed only marginally, the high-speed streaks near the wall have undergone a breakdown into two streaks, the process being completed by $t=156$ as shown in Figs. 5.9 and 5.10.

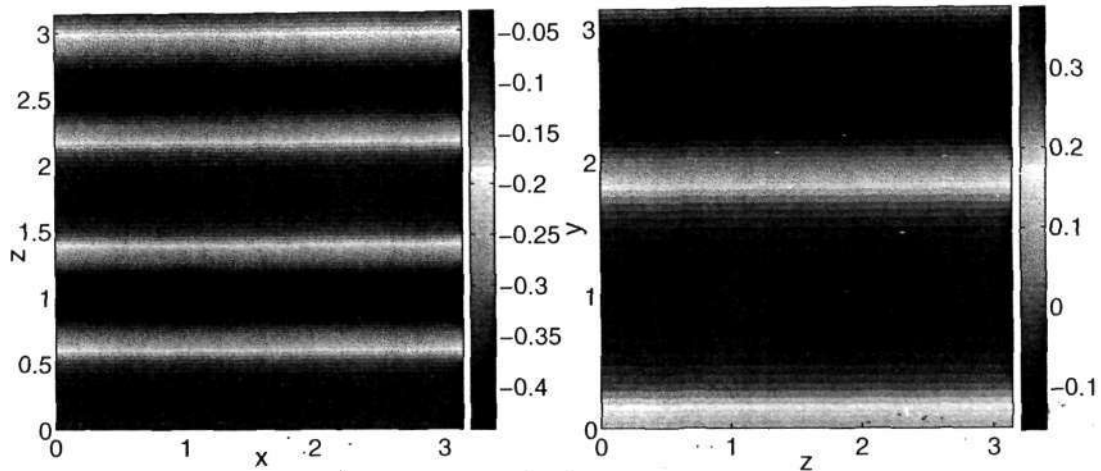
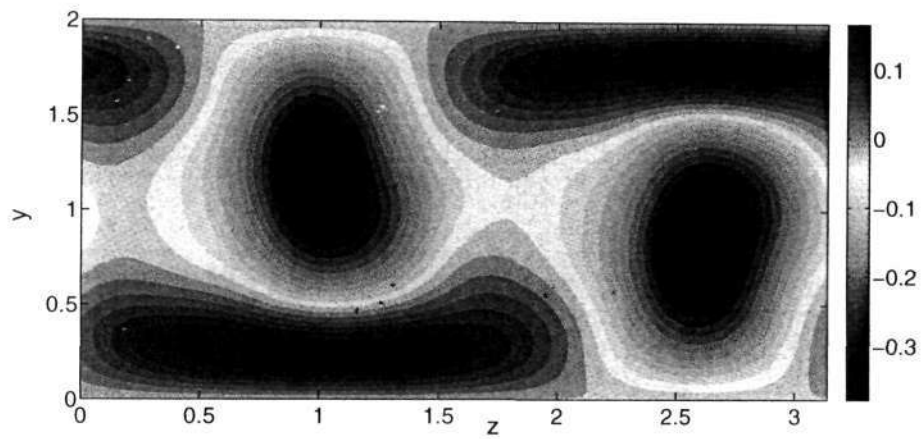
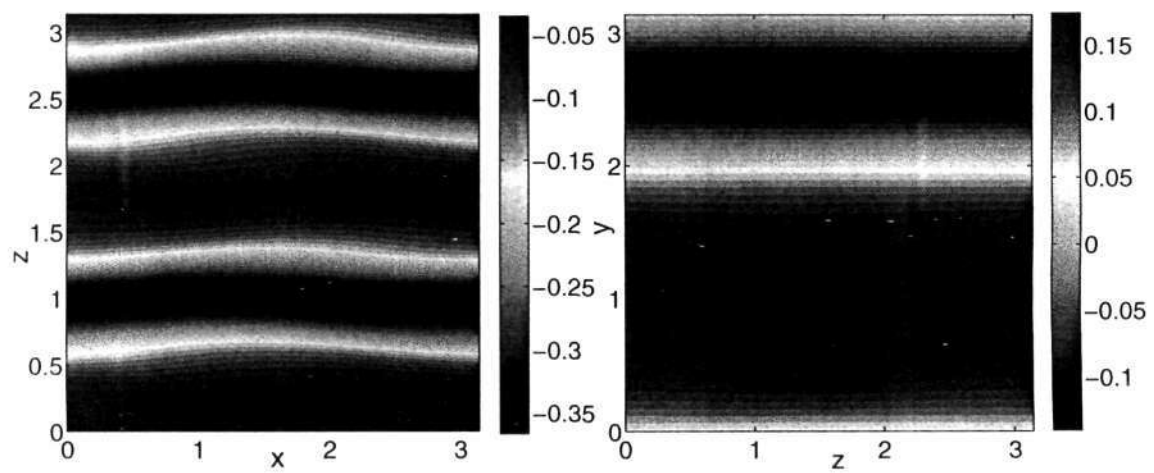
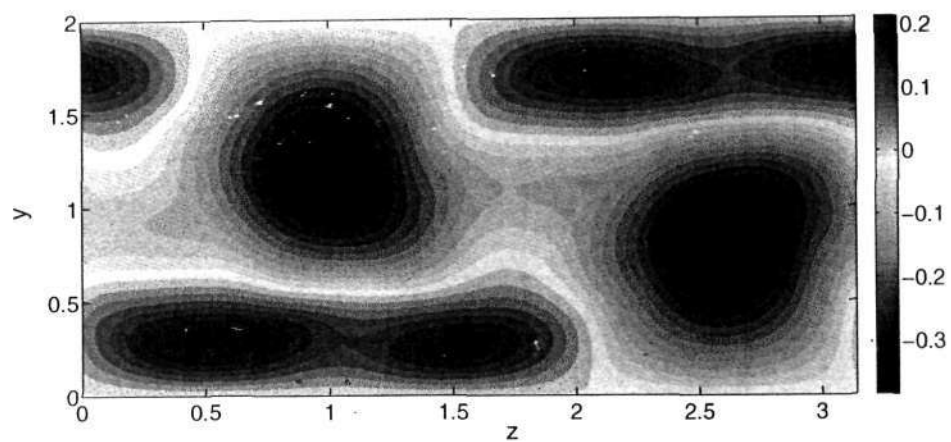
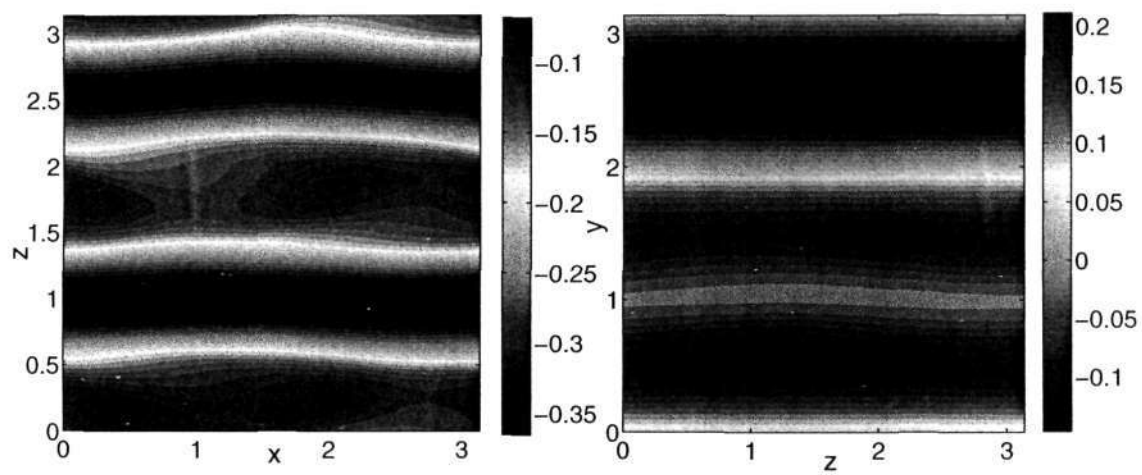


Figure 5.4: Contours of the streamwise velocity with the mean subtracted at $t=24$, in two $x - z$ planes given by $y=L_y/2$ (left) and $y=L_y/6$ (right). The x - direction is along the horizontal. Here $Re=1000$ and $Gr=0$

The first leg of the energy increase corresponds to the instability of the high-speed near-wall streak which causes the formation of other streaks with lesser mutual spacing. This is not entirely surprising.

The measure of streak spacing along the z - direction, in transitional and turbulent flow has seen considerable controversy over the past few years. Results from experiments and numerical simulations have shown that in *turbulent* flow, the streak spacing seems to be in the vicinity of 100 wall units (a length scale defined on the averaged near wall turbulent shear stress) for many different wall-bounded flows including channel flow, Couette flow and boundary layer flow. Butler & Farrell (1993) had considered the possibility that the streak spacing observed from optimal perturbations (corresponding to Fig.5.3) are close to that observed in turbulent flows. A withering criticism by Waleffe (1995*a,b*) followed who showed that the streaks observed in turbulent flows are of a particular kind which, after breakdown, *regenerate* the streamwise vortices that originally generate them through the lift-up mechanism. A recent paper by Jimenez & delAlamo (2006) realized that if instead of looking for optimal perturbations to the laminar parabolic profile, one considers the mean *turbulent* profile, one obtains exactly the streak spacing of 100 wall units observed in near wall turbulent flow. A detailed study of evolution of

Figure 5.5: Same as Fig. 5.3 but at $t=67$ Figure 5.6: Same as Fig. 5.4 but at $t=67$

Figure 5.7: Same as Fig. 5.3 but at $t=93.6$ Figure 5.8: Same as Fig. 5.4 but at $t=93.6$

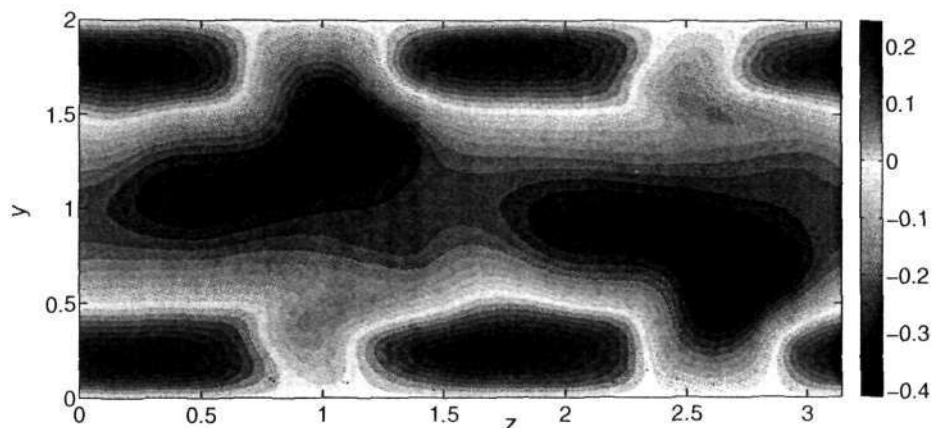
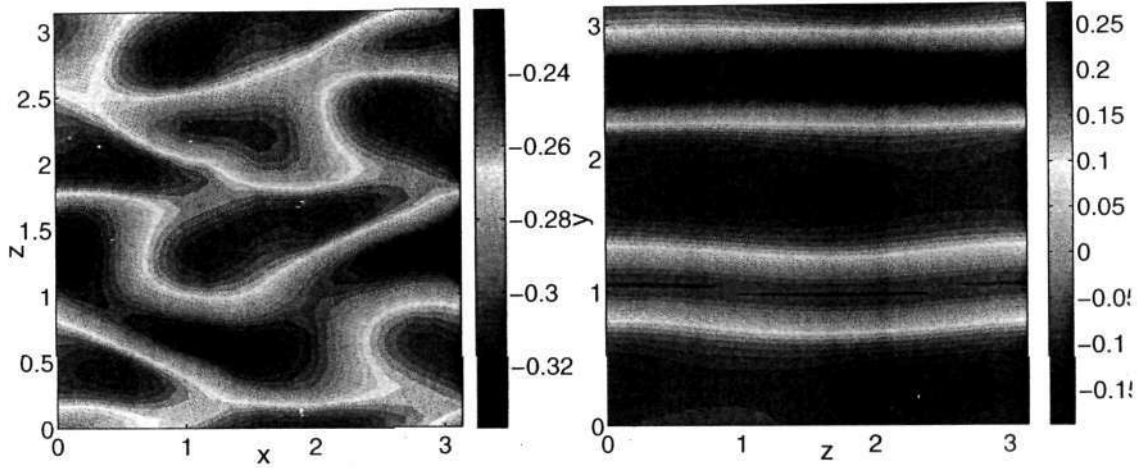


Figure 5.9: Same as Fig. 5.3 but at $t=156$

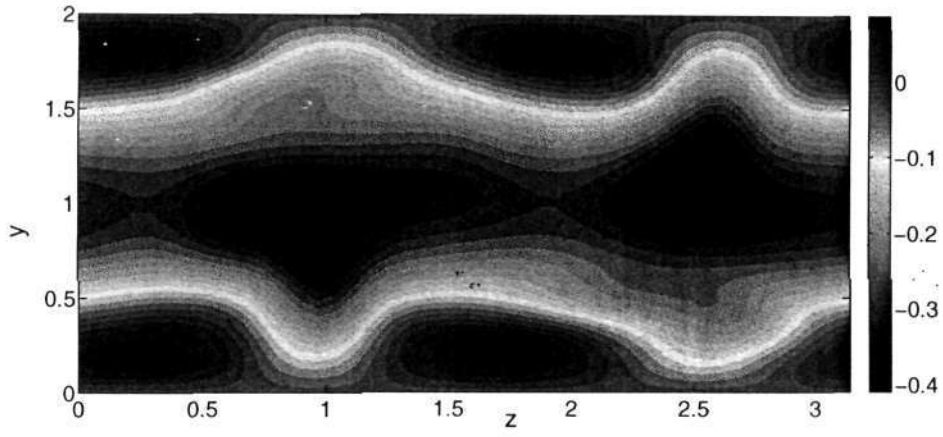
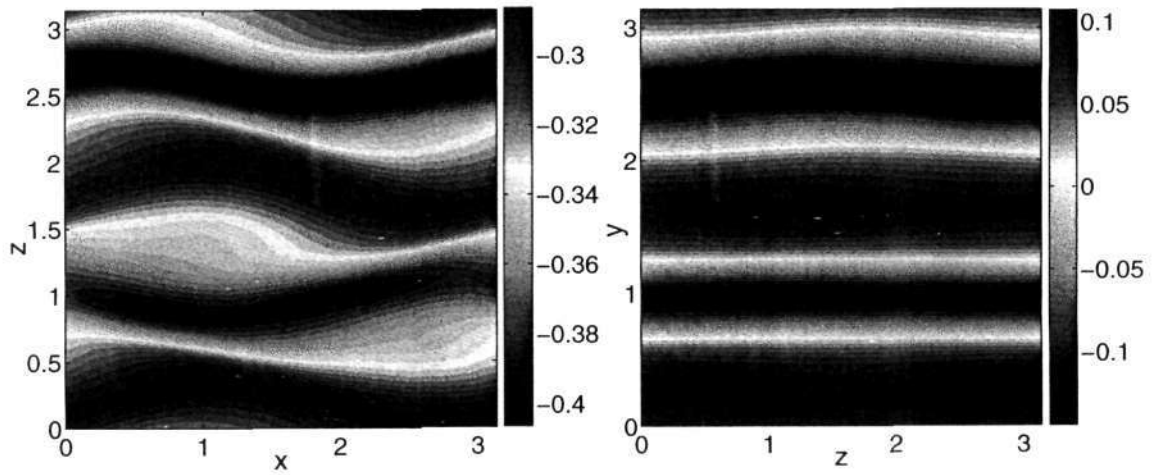
the streak spacing from optimal perturbations (of laminar parabolic flow) to that in turbulent flow is not something we have been able to find in existing literature. But the aforementioned studies seem to indicate that the near wall streak spacing in turbulent flow is in fact different from that observed in streaks generated from laminar optimal perturbations. The breakdown of near wall streaks in the first leg of the energy growth in Fig 5.2 and shown in Figs. 5.7 and 5.9 might be related to the process of ‘choosing’ the streak spacing. One of the obstacles in undertaking a detailed study of this mechanism is that it entails much larger domain sizes along the x - and z - directions (and consequently a much higher number of Fourier modes along these directions to maintain the same numerical resolution used here). This is because the periodicity of the domain in these directions inherently forces any flow quantity (for example the streak spacing) to exist in integral multiples of the periodic length (L_x and L_z in this case). A much larger domain length along these directions would be needed to ensure that the flow naturally chooses the streak spacing rather than being forced so by the domain periodicity. However, such a study is well beyond our present computational capabilities and shall be reserved for future studies.

The contour plots from a time in the second leg, at $t=156$ (in Figs. 5.9 and 5.10) show the instability and breakdown of the low-speed streaks near the channel center and this is what causes the spurt in the disturbance energy. By $t=240$, Figs 5.9 and 5.10 indicate that the streak instability starts to die down and the streak structure

Figure 5.10: Same as Fig. 5.4 but at $t=156$

(defined by localized regions of streamwise velocity) has started to be disrupted by the homogenizing action of dissipation towards the laminar parabolic profile. The optimal perturbations for $Re=1000$ therefore cause transition to a different temporary unsteady state but not transition to turbulence. However, as remarked previously, studies on much larger domain sizes, L_x and L_z (and consequently larger N_x and N_z) are needed to study this aspect better.

Next we consider the same flow situation as the previous one with added stratification, the Grashof number being 200 which corresponds to Chapter 3, Fig. 3.2 c) with all other parameters being the same. The optimal perturbation for this case is computed from linear theory and used as a starting point for the DNS code. We plot the streamwise velocity contours as in the previous case and at the same non-dimensional times in the figures 5.13 - 5.21. As we examine the evolution of evolution and instability of the streaks in time, we observe considerable similarity in the evolution of both the unstratified and the stratified cases. Even here, the streak instability seems to proceed at the corresponding times in two legs, corresponding to the instability of the high-speed and low-speed streaks in that order. The streak spacing and the structure of the near wall streaks after the first instability is seen to be similar in the stratified and unstratified cases. Further, comparisons between Figs. 5.5 and 5.15 first and then 5.7 and 5.17 indicate that the nature of the in-

Figure 5.11: Same as Fig. 5.3 but at $t=240$ Figure 5.12: Same as Fig. 5.4 but at $t=240$

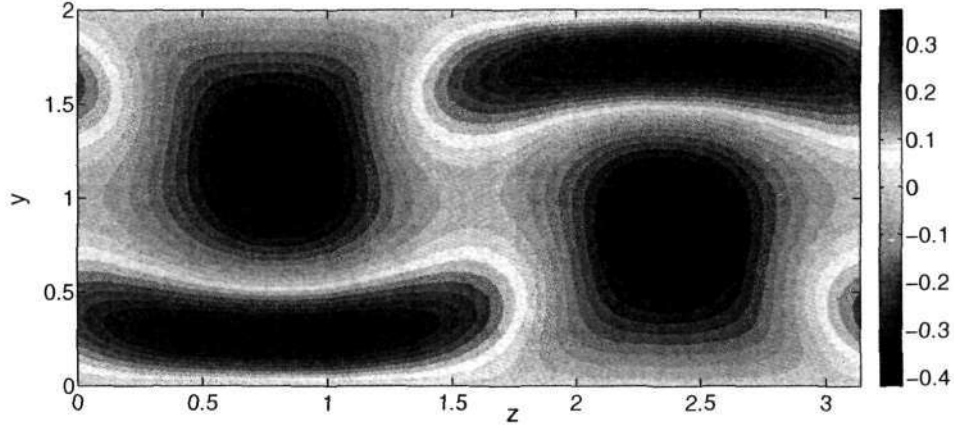


Figure 5.13: Contours of the streamwise velocity with the mean subtracted at $t=24$, in the $y-z$ plane, $x=L_x/2$ with the z -direction being along the horizontal. Here $Re=1000$ and $Gr=200$.

stability process and the time at which it occurs is not particularly affected. The stratified case however seems to take longer to reach the stable laminar state as seen in Fig. 5.22.

In order to get a better understanding of the comparison between the stratified and unstratified cases, we consider the energy of evolution of the flow vs time, as in the case of Fig. 5.2. Note that the energy for the stratified case consists of a kinetic energy term and a potential energy term due to buoyancy. In Fig. 5.23, we plot the total energy, kinetic energy, $(\int_V (|u^2| + |v^2| + |w^2|) dV)$ the potential energy $(\int_V |T^2| dV)$ and the $Gr=0$ case already plotted in Fig. 5.2 as a reference. The most important observation is that the evolution of the kinetic energy term with stratification present is only marginally different from the corresponding unstratified case for this value of (α, β) . In fact the maximum disturbance energy attained *after* the onset of the instability is actually *lesser* now. Further the potential energy evolution shows that, other than the initial transient growth, which is due to the lift-up mechanism, the temperature field does not gain from the mean background field during the instability process. From this preliminary study it seems, rather paradoxically, that the presence of the unstable stratification has marginally stabilized the streak instability process. Note that our inability to repeat the study for higher periodic lengths along the x - and z -directions limits our ability

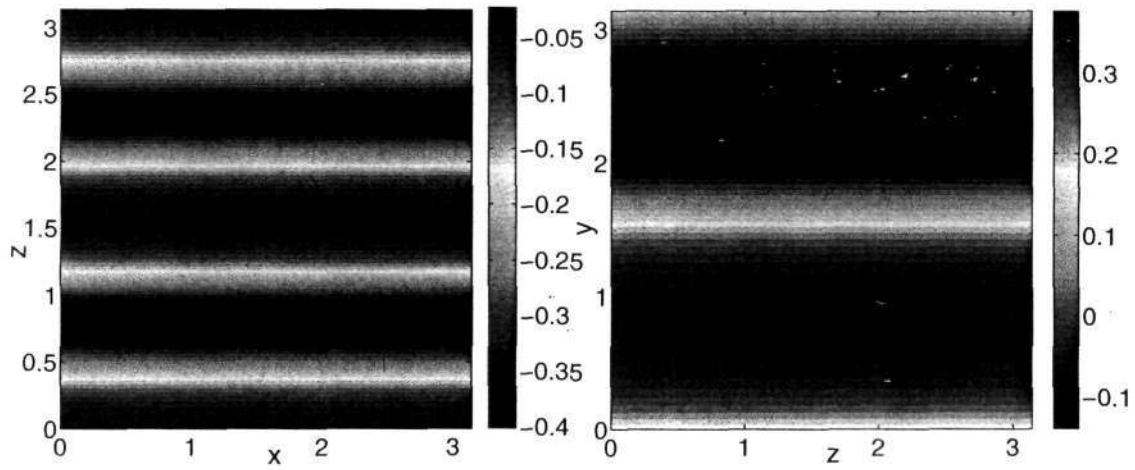


Figure 5.14: Contours of the streamwise velocity with the mean subtracted at $t=24$, in two $x-z$ planes given by $y=L_y/2$ (left) and $y=L_y/6$ (right). The x -direction is along the horizontal. Here $Re=1000$ and $Gr=200$.

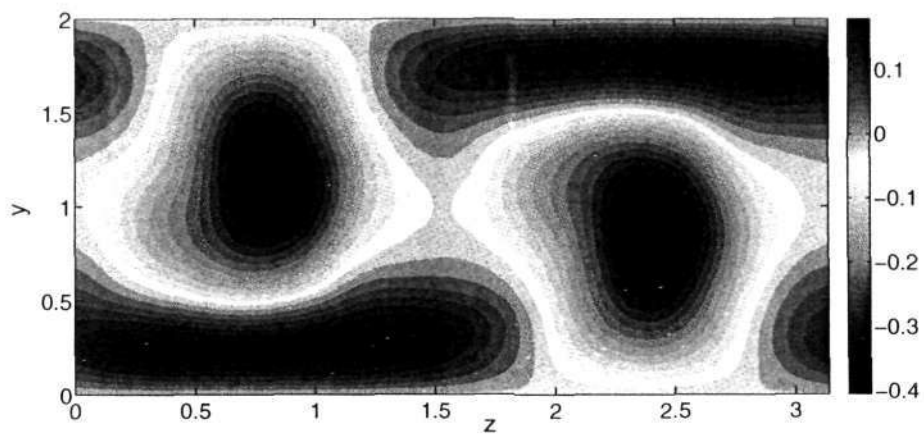
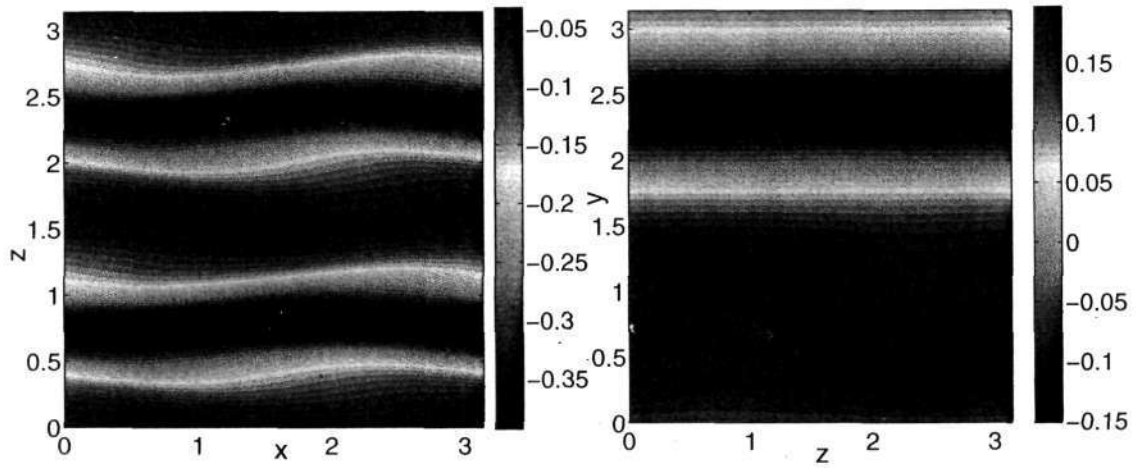
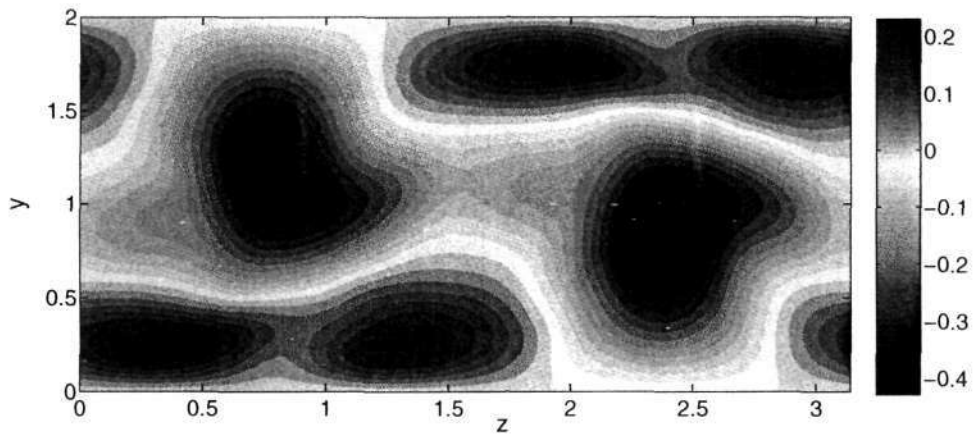


Figure 5.15: Same as 5.13 but at $t=67$.

Figure 5.16: Same as 5.14 but at $t=67$.Figure 5.17: Same as 5.13 but at $t=93$.

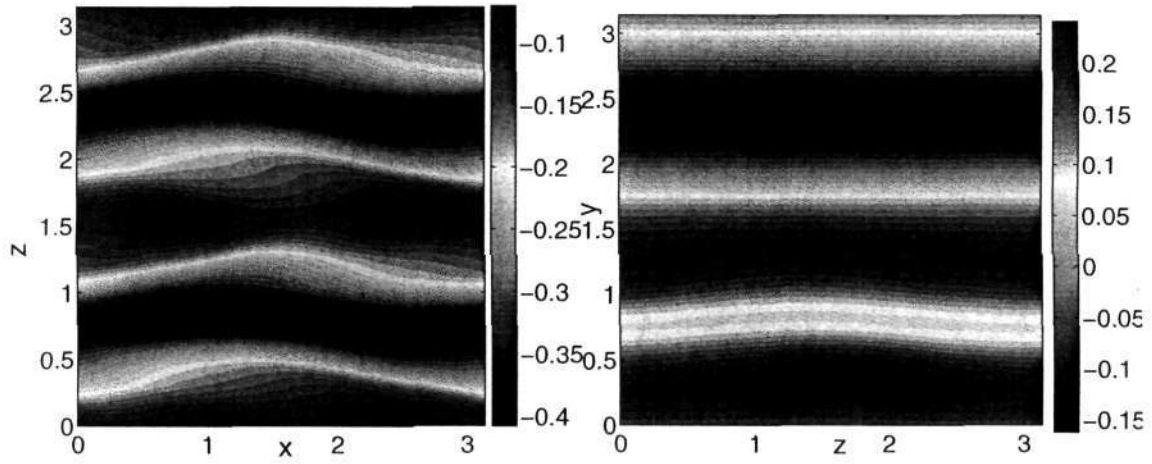


Figure 5.18: Same as 5.14 but at $t=93$.

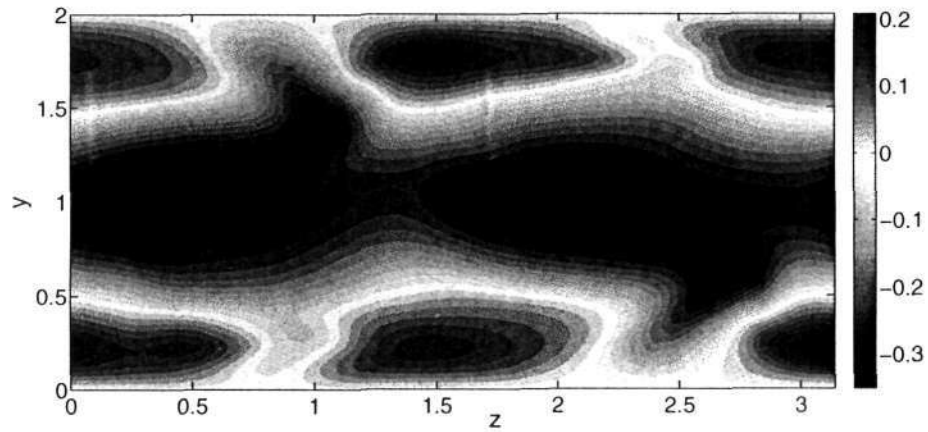
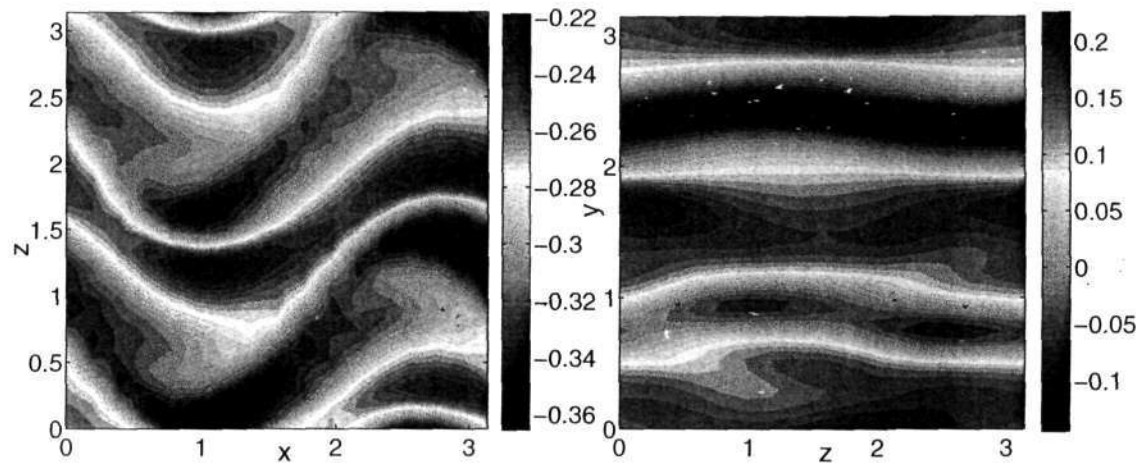
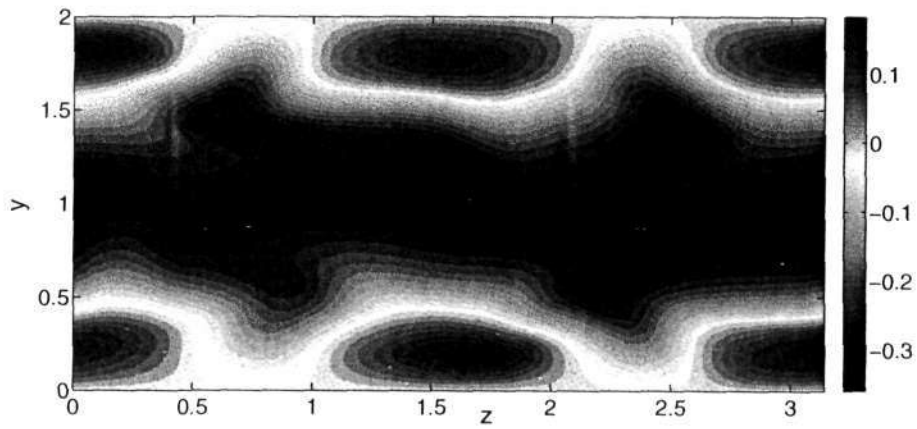


Figure 5.19: Same as 5.13 but at $t=156$.

Figure 5.20: Same as 5.14 but at $t=156$.Figure 5.21: Same as 5.13 but at $t=240$.

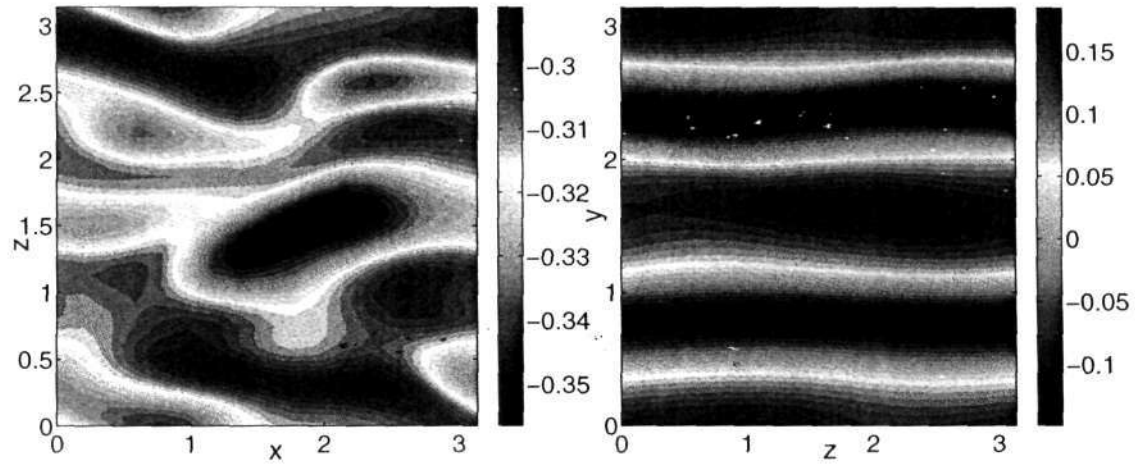


Figure 5.22: Same as 5.14 but at $t=240$.

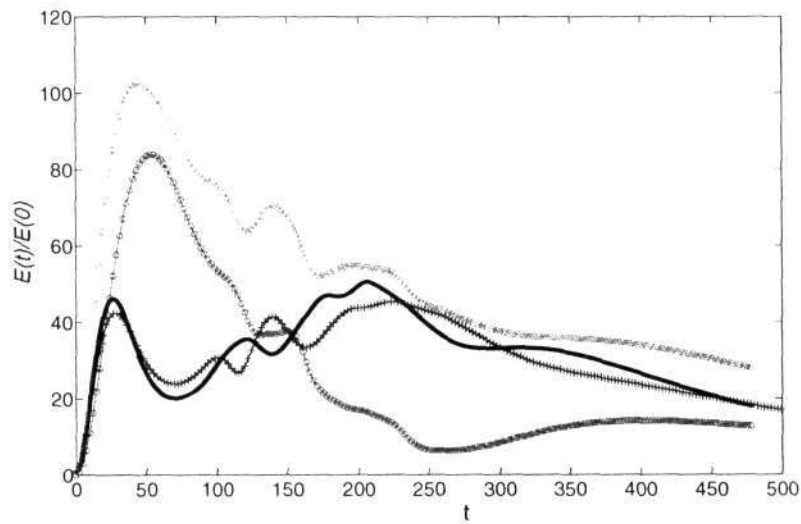


Figure 5.23: Evolution of the normalized disturbance energy, $E(t)/E(0)$ with time for the optimal disturbance at $Re=1000$ and $Gr=200$ ($\alpha = 0, \beta = 2$). The red, green and black curves show the evolution of the potential energy, total energy and kinetic energy respectively. The blue curve is the kinetic energy evolution for the unstratified case and has already been plotted in Fig. 5.2

to draw detailed inferences from the results that we have obtained. In particular, we had noticed in chapter 3 that the most unstable spanwise wave number, β , shifts continuously and rapidly as the Grashof number is increased. In spite of these limitations, some aspects of the physics of the problem can be speculated upon from the results we have obtained. Some insight can be gained from the paper by Bakas *et al.* (2001), where the authors consider transient growth of plane waves in an unbounded uniform shear flow in the presence of stable stratification. At one point they remark, “*It should be noted that the vertical velocity in a stratified flow induces density perturbations, which if large, can lead to unstable density stratification that can cause collapse of the plane wave by convective overturning. This process limits the validity of the perturbation equations...*”. The statement here reflects the possibility of regions of local *unstable* stratification in a stably stratified fluid when optimal perturbations are imposed. The opposite phenomenon seems to occur for the wavelength chosen, essentially that the optimal perturbations can cause stabilization by inducing regions of stable stratification. This can be easily observed by considering the structure of the temperature streaks in Chapter 3, Fig. 3.6. The counter-rotating streamwise vortices which constitute the optimal perturbations advect hot fluid towards the cold wall and cold fluid towards the hot wall. This causes a net homogenization of the temperature and a reduction of the vertical unstable gradient, therefore causing a possible stabilization. An interesting parallel to this phenomenon occurs in Rayleigh-Benard convection, where the flow undergoes an instability from a base state of stationary fluid with unstable density stratification to a secondary state involving *stable* convection rolls which are in the form of counter-rotating vortices. The stability of the convection rolls is aided by a reduction in the mean unstable temperature gradient by precisely the mechanism mentioned above for the streamwise-vortices in channel flow. A reasonable possibility therefore exists that the action of the initial perturbation through the lift-up process on temperature might tend to balance the effects of a mean unstable stratification to some extent. To actually quantify this point would require a stability analysis of the velocity streak profile with the corresponding temperature streak profile being considered. This would be an extension of the approach of Reddy *et al.* (1998) but is beyond the scope of the work presented here.

Another reason for the lack of destabilization by the unstable stratification is the low value of the Richardson number. The vertical velocity equation is forced by

the temperature term linearly, as a consequence of the Boussinesq approximation through a factor of Ri . The lift-up temperature effect occurs because of the action of vertical velocity on the temperature and is as such independent of the Richardson number. A higher value of Ri would only marginally change the lift-up but could contribute significantly to the instability process. This point is moot however, as a higher value of Richardson number would cause linear instability to be active as shown in Fig. 5.2 *d*).

One possibility that could weaken the possible explanations suggested in the previous paragraphs is that the streak instability process significantly disrupts the transient stable stratification induced by the lift-up mechanism. This could be a purely advective process and is possible, because the symmetries of the velocity streaks differs from that of the temperature streaks as explained in the final section of Chapter 3. We therefore plot the contours of the temperature field in two planes, an $x - z$ plane bisecting the channel center and a $y - z$ plane at the same times marked in Fig. 5.2. As we observe the evolution of the temperature at different times, we see that the structure of the low and high temperature blobs are not significantly disrupted in a fashion that might reduce the effect of the original stable stratification zones that occur due to temperature lift-up. At $t=240$, when the instability has begun to subside, the temperature streaks seem to break-up in a manner similar to the velocity breakup with lesser mutual spacing. However the streak structure *still* maintains the stable configuration.

We thus see the transition occurring from optimal disturbances occurs in two stages, the first involving the formation of streaks through lift-up and the second where the actual instability of streaks. To judge the outcome of the second stage of transition merely by measuring the magnitude of transient growth might not be appropriate as the previous results indicate. Here the transient growth in the total energy with stratification added is twice of that in the unstratified case for $Gr=200$ but the streak instability process is largely unaffected. We have conducted computations for a higher value of the Reynolds number, $Re=1500$ for the cases, $Gr=0$ and $Gr=200$. Here the transition of the streaks is more violent but the observations are essentially the same as that observed for the case of $Re=1000$.

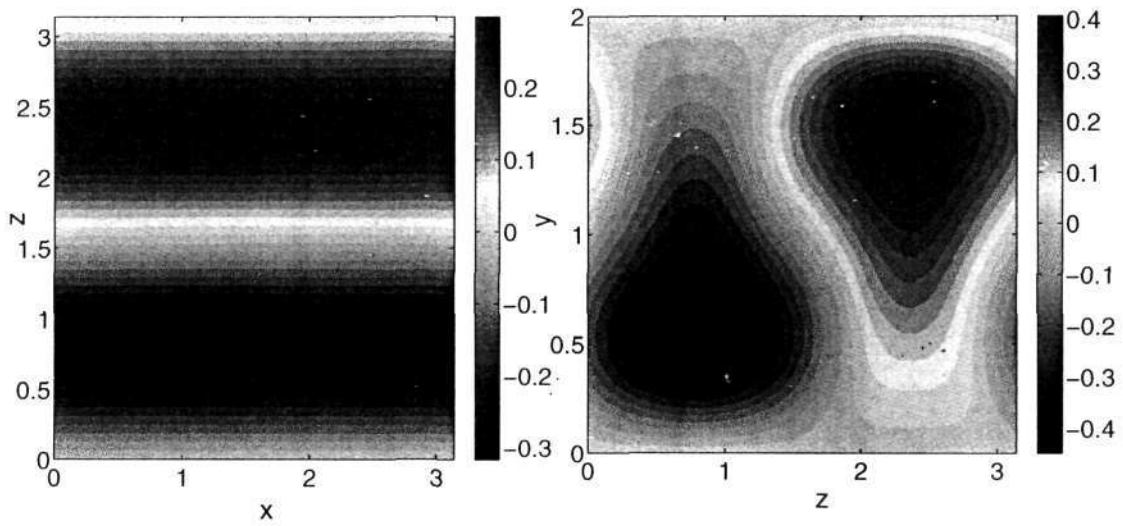


Figure 5.24: Contours of the temperature, T in the (left) $x-z$ plane at $y=L_y/2$ and (right) in the $y-z$ plane. The horizontal direction in the left and right figure is the x - and z - direction respectively. Here $t=24$.

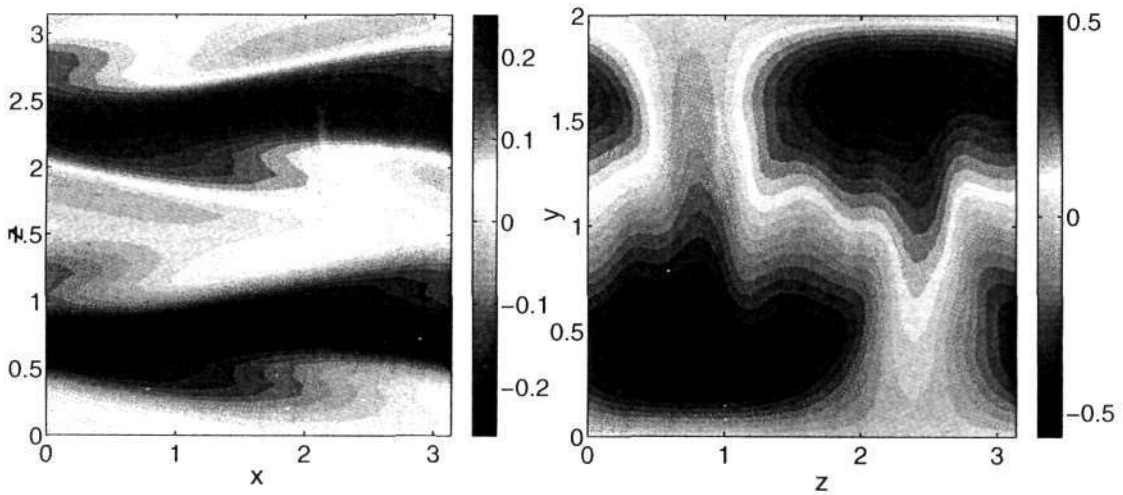


Figure 5.25: Same as Fig. 5.24. But at $t=67$.

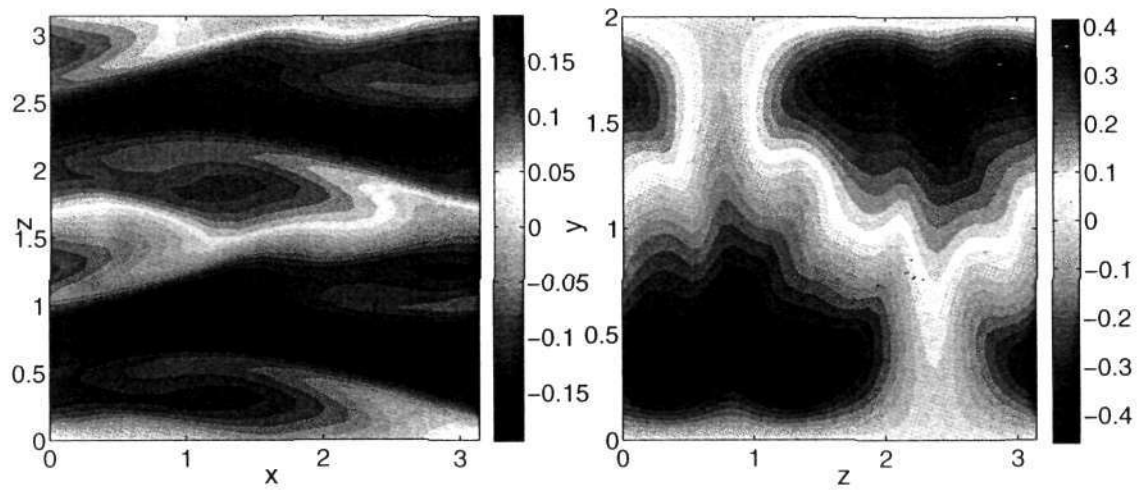


Figure 5.26: Same as Fig. 5.24. But at $t=93$.

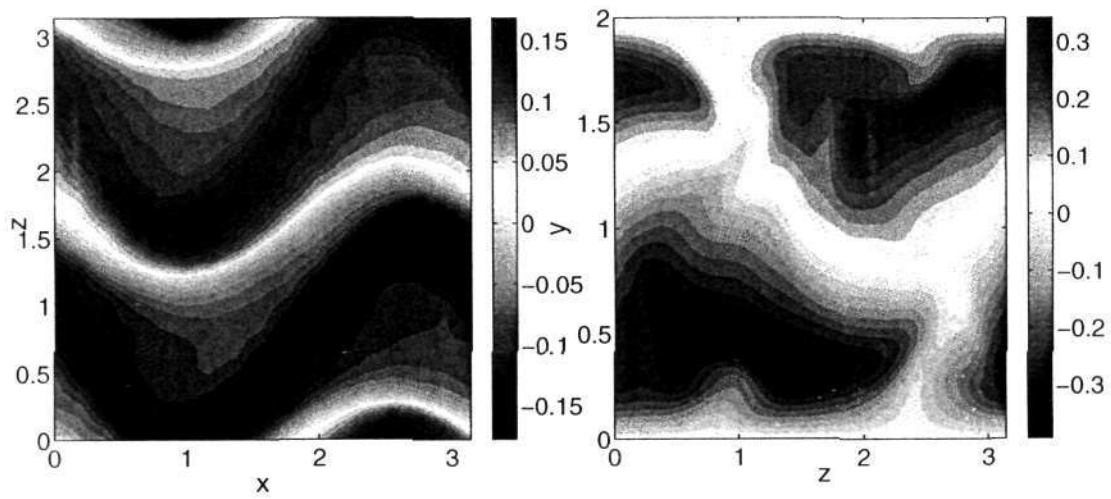
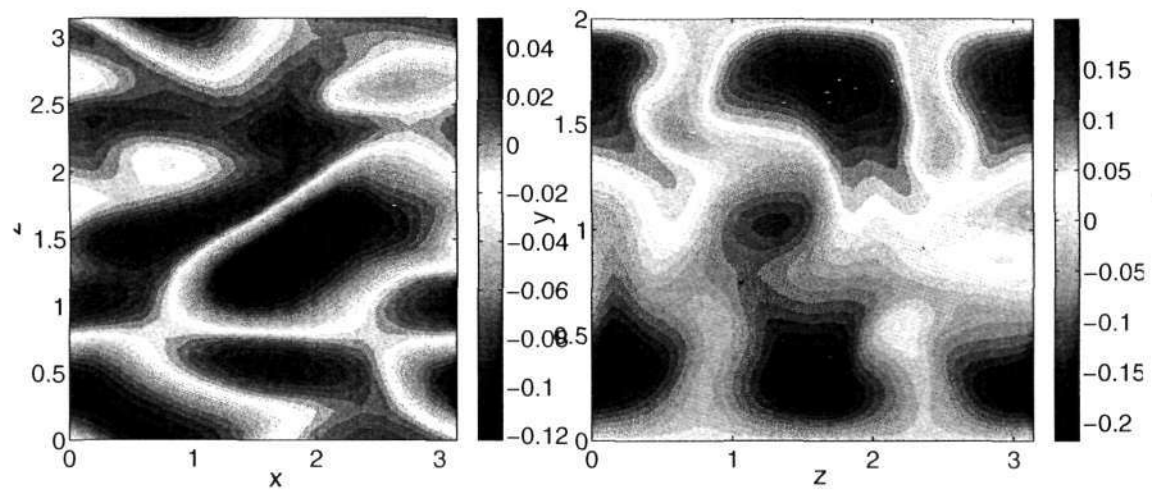


Figure 5.27: Same as Fig. 5.24. But at $t=156$.

Figure 5.28: Same as Fig. 5.24. But at $t=240$.

CHAPTER 6

CONCLUSIONS AND FUTURE OUTLOOK

Our present study is aimed at understanding the mechanism of transition in an unstably stratified channel flow due to algebraic growth. The class of initial perturbations that we start with are those which cause maximum transient growth from the purview of linear theory. These optimal perturbations are in the form of streamwise vortices and cause transient growth using the lift-up mechanism which involves redistribution of the mean shear by vortices. The redistribution of shear causes the formation of streaks, which are regions of high and low speed flow relative to the background parabolic mean profile. In our present study we find that the vortices not only distribute mean shear, but the mean temperature too, causing the formation of high and low temperature 'streaks'. The structure of the temperature streaks are found to be different than that of the velocity streaks primarily because of the difference in symmetry of the temperature and velocity mean profiles, which are anti-symmetric and symmetric about the channel centerline, respectively.

We find that starting with finite-amplitude optimal perturbations, the flow at a Reynolds number of 1000 undergoes transition to a different temporary unsteady state, but not transition to turbulence. In particular we identify the streak instability mechanism which involves two stages that can be identified by the two distinct spurts in the evolution of the disturbance energy in time. The first of these stages involves the high-speed near-wall streaks undergoing instability, causing them to break up into streaks with lesser near-wall spacing. The second stage involves the instability of the low-speed streaks, the completion of which causes the flow to return to the original laminar profile. On adding unstable stratification quantified by a Grashof number of 200, and repeating the computation, we find that the physical process of the streak instability is not particularly affected. Further, by observing the evolution of the kinetic energy with and without the presence of stratification, we find that there is only a marginal change in the latter case, relative to the former. This observation is corroborated by the evolution of the potential energy which does not undergo any increase that might indicate that the temperature perturbation term gains energy from the background buoyant profile. One of the

possible reasons we have considered for this observation is that the structure of the temperature streaks is stabilizing in nature. This occurs because of the action of the counter-rotating streamwise vortices which move fluid from the hotter to the colder and vice-versa causing a reduction in the mean unstable stratification.

However the above observations and inferences must be considered with caution because of the restrictions imposed on the evolution of the instability due to the periodicity of the flow imposed by our computations in the streamwise and spanwise directions. In particular this might strongly affect the streak instability process which causes the formation of streaks of smaller spacing. We find that the spacing after instability is essentially half of the existing spacing. It is clear that this specific choice of the spacing is an artifact of the periodicity. The same reasons might also affect the lack of noticeable change in the instability mechanism in the presence of stratification. Unless the computations are repeated for higher domain lengths in the periodic directions, any inferences drawn from the present preliminary computations are speculative at best. Any future work must therefore involve increasing the domain lengths to many times the existing one to allow a choice of the streak spacing after the first instability. Further, a careful study of the streak instability process needs to be done using the approach in Reddy *et al.* (1998) where the authors initially compute the mean distorted profile due to streak formation and perform a stability analysis of the resulting profile. Performing the same stability analysis with stratification included is essential to corroborating the DNS results.

Another aspect to be considered is the effect of viscosity stratification and buoyancy on the nonlinear evolution of optimal perturbation. The investigations of Sameen & Govindarajan (2007) show a fundamentally different character in the observed transient growth at moderate Prandtl numbers ($\sim O(1)$). This study was in fact conceived as a first step in studying the more complex problem of viscosity stratification added and we hope to do the same in future.

References

- BAKAS, N., IOANNOU, P. & KEFALIAKOS, G. 2001 The emergence of coherent structures in stratified shear flow. *J. Atmos. Sci.* **58**, 2790–2806.
- BIAU, D. & BOTTARO, A. 2004 The effect of stable thermal stratification on shear flow instability. *Phys. Fluids* **16**(14), 4742–4745.
- BROWNING, K. & LUDLAM, F. 1962 Airflow in convective storms. *Quat. J. Roy. Meteor. Soc.* **88**, 117.
- BUTLER, K. M. & FARRELL, B. F. 1992 Three-dimensional optimal perturbations in viscous shear flow. *Phys. Fluids* **4**(8), 1637–1650.
- BUTLER, K. M. & FARRELL, B. F. 1993 Optimal perturbations and streak spacing in wall-bounded shear flow. *Phys. Fluids* **5**(3), 774–777.
- CARRIERE, P. & MONKEWITZ, P. 1999 Convective versus absolute instability in mixed rayleigh-benard-poiseuille convection. *J. Fluid Mech.* **384**, 243–262.
- CHANDRASEKHAR, S. 1961 *Hydrodynamics and hydromagnetic stability*. Oxford University Press, London.
- CHIMONAS, G. 1979 Algebraic disturbances in stratified shear flows. *J. Fluid Mech* **90**, 1–19.
- CHORIN, A. 1968 Numerical solution of the navier-stokes equations. *Math. Comput.* **22**, 745.
- CLEVER, R. & BUSSE, F. 1991 Instabilities of longitudinal rolls in the presence of Poiseuille flow. *J. Fluid Mech.* **229**, 517–529.
- COLES, D. 1965 Transition in circular couette flow. *J. Fluid Mech* **21**, 385.
- FARRELL, B. & IOANNOU, P. 1993 Transient development of perturbations in stratified shear flow. *J. Atmos. Sci.* **50**, 2201–2214.
- FARRELL, B. & IOANNOU, P. 1996 Generalized stability theory. part 1 : Autonomous operators. *J. Atmos. Sci.* **53**, 2025–2040.

- FARRELL, B. F. 1988 Optimal excitation of perturbations in viscous shear flow. *Phys. Fluids* **31**, 2093–2102.
- GAGE, K. & REID, W. 1968 The stability of thermally stratified plane poiseuille flows. *J. Fluid Mech.* **33**, 21.
- HAMILTON, J., KIM, J. & WALEFFE, F. 1995 Regeneration mechanisms of near-wall turbulence structures. *J. Fluid Mech.* **287**, 317–348.
- HERBERT, T. 1983 Secondary instability of plane channel flow to subharmonic three-dimensional disturbances. *Phys. Fluids* **26**(4), 871–874.
- HOF, B., VAN DOORNE, C. W. H., WESTERWHEEL, J., NIEUWSTADT, F., FAISST, H., ECKHARDT, B., WEDIN, H., KERSWELL, R. & WALEFFE, F. 2004 Experimental observations of nonlinear travelling waves in turbulent pipe flow. *Science* **305**, 1594–1598.
- JIMENEZ, J. & DELALAMO, J. 2006 Linear energy amplification in turbulent channels. *J. Fluid Mech.* **559**, 205–213.
- JIMENEZ, J. & PINELLI, A. 1999 The autonomous cycle of near-wall turbulence. *J. Fluid Mech.* **389**, 335–359.
- JOSEPH, D. D. 1976 *Stability of Fluid Motions I*, 1st edn. Springer-Verlag.
- KERSWELL, R. 2005 Recent observations in transition to turbulence in pipe flow. *Nonlinearity* **18**, R17–R44.
- KIM, J. & MOIN, P. 1985 Application of a fractional-step method to incompressible navier-stokes equations. *J. Comp. Phys.* **59**, 308.
- KLEISER, L. & SCHUMANN, U. 1980 Treatment of incompressibility and boundary conditions in 3-d numerical spectral simulations of plane channel flows. *Conference on Numerical Methods in Fluid Mechanics, 3rd, Cologne, West Germany, October 10-12, 1979, Proceedings. (A80-38252 15-34) Braunschweig, Friedr. Vieweg und Sohn Verlagsgesellschaft mbH* pp. 165–173.
- LANDAHL, M. T. 1980 A note on an algebraic instability of inviscid parallel shear flows. *J. Fluid Mech* **98**(2), 243–251.
- LEE, M. J., OH, B. D. & KIM, Y. B. 2001 Canonical fractional-step methods and consistent boundary conditions for the incompressible navier stokes equations. *J. Comp. Phys.* **168**, 73–100.
- LELE, S. K. 1992 Compact finite difference schemes with spectral-like resolution. *J. Comp. Phys.* **103** (1), 16.

- LIPPS, F. 1971 Two-dimensional numerical experiments in thermal convection with vertical shear. *J. Atmos. Sci.* **28**, 3–18.
- LIU, M., REN, Y. & ZHANG, H. 2004 A class of fully second order accurate projection methods for solving the incompressible navier stokes equations. *J. Comp. Phys.* **200**, 325–346.
- NISHIOKA, M., IIDA, S. & ICHIKAWA, Y. 1975 An experimental investigation of the stability of plane Poiseuille flow. *J. Fluid Mech.* **72**, 731–751.
- ORR, W. M. 1907 The stability or instability of the steady motions of a perfect liquid and of viscous liquid. *Proc. Roy. Irish Acad. A* **27**, 9–138.
- RAI, M. & MOIN, P. 1991 Direct simulations of turbulent flow using finite-difference schemes. *J. Comp. Phys.* **96**, 15–53.
- REDDY, S. C. & HENNINGSON, D. S. 1993 Energy growth in viscous channel flows. *J. Fluid Mech* **252**, 209–238.
- REDDY, S. C. & HENNINGSON, D. S. 1994 On the role of linear mechanisms in transition to turbulence. *Phys. Fluids* **6**, 1396.
- REDDY, S. C., SCHMID, P. J., BAGGET, J. S. & HENNINGSON, D. S. 1998 On stability of streamwise streaks and transition thresholds in plane channel flows. *J. Fluid Mech.* **365**, 269–303.
- SAMEEN, A. 2004 *Stability of Plane Channel Flow with viscosity stratification*. Phd Thesis, Department of Aerospace Engineering, Indian Institute of Science.
- SAMEEN, A. & GOVINDARAJAN, R. 2007 The effect of wall heating on instability of channel flow. *J. Fluid Mech.* **577**, 417–442.
- SCHMID, P. J. & HENNINGSON, D. S. 2001 *Stability and Transition in Shear Flows*. Springer-Verlag, New York.
- SENGUPTA, T. K. 2004 *Fundamentals of Computational Fluid Dynamics*, 1st edn. University Press.
- TREFETHEN, L. N., TREFETHEN, A. E., REDDY, S. C. & DRISCOLL, T. A. 1993 Hydrodynamic stability without eigenvalues. *Science* **261**, 578.
- WALEFFE, F. 1995a Hydrodynamic stability and turbulence: Beyond transients to a self-sustaining process. *SIAM* **95**, 319–343.
- WALEFFE, F. 1995b Transition in shear flows. Nonlinear normality versus non-normal linearity. *Phys. Fluids* **7**, 3060.

15/1/14

WEISMAN, M. & KLEMP, J. 1982 The dependence of numerically simulated convective storms on vertical wind shear and buoyancy. *Month. Wea. Rev.* **110**, 504.

WILHELMSON, R. & KLEMP, J. 1981 A three dimensional analysis of splitting severe storms on 3 april 1964. *J. Atmos. Sci.* **38**, 1581.

532.51
p07